2017

Amyloid Fibril Nucleation In Reverse Micelles

Gozde Eskici
University of Pennsylvania, geskici@mail.med.upenn.edu

Recommended Citation

Eskici, Gozde, "Amyloid Fibril Nucleation In Reverse Micelles" (2017). *Publicly Accessible Penn Dissertations*. 2272.
https://repository.upenn.edu/edissertations/2272

Amyloid Fibril Nucleation In Reverse Micelles

Abstract
The 40-residue amyloid beta protein (Abeta) is the unstructured cleavage product of a common membrane protein that is produced in large quantities, but normally cleared from the brain before it exerts any apparent toxicity. Under some conditions, however, it undergoes a conformational change and aggregates into fibrils. These fibrils then coalesce into amyloid plaques, which are the pathognomonic brain lesions of Alzheimer's disease. The plaques are centers of active oxidative stress and neuronal death, so the conditions under which fibrils form is of high interest. When Abeta is encapsulated in a reverse micelle, its infrared spectrum indicates that it spontaneously adopts a fibril-like structure, which is remarkable because only one Abeta strand is present in each reverse micelle. That observation suggests that some aspect of the reverse micelle environment such as crowding, dehydration, proximity to a membrane, or high ionic strength may induce Abeta to nucleate amyloid fibril formation. Therefore, an understanding of the factors that induce Abeta to adopt fibril-like structure in reverse micelles may reveal what causes amyloid fibrils to form in Alzheimer's disease. Molecular dynamics simulations of Abeta in reverse micelles have been performed to identify and understand these factors. Results indicate that Abeta side chains penetrate the reverse micelle surface, anchoring the peptide in the membrane. Other interactions between peptide and membrane stabilize intrachain hydrogen bond formation and secondary structure. These interactions may be important factors in the formation of amyloid fibrils and the pathogenesis of Alzheimer's disease.

Degree Type
Dissertation

Degree Name
Doctor of Philosophy (PhD)

Graduate Group
Biochemistry & Molecular Biophysics

First Advisor
Paul H. Axelsen

Keywords
Alzheimer's Disease, Amyloid beta, Fibril nucleation, Molecular Dynamics Simulations, Reverse micelles

Subject Categories
Biochemistry | Biophysics

AMYLOID FIBRIL NUCLEATION IN REVERSE MICELLES

Gözde Eskici
A DISSERTATION

in

Biochemistry & Molecular Biophysics

Presented to the Faculties of the University of Pennsylvania

in

Partial Fulfillment of the Requirements for the

Degree of Doctor of Philosophy

2017

Supervisor of Dissertation

Paul H. Axelsen, M.D., Professor of Pharmacology

Graduate Group Chairperson

Kim Sharp, Ph.D., Associate Professor of Biochemistry & Biophysics

Dissertation Committee

Kim Sharp, Ph.D., Professor of Biochemistry & Biophysics
Elizabeth Rhoades, Ph.D., Associate Professor of Chemistry
Ravi Radhakrishnan, Ph.D., Professor of Bioengineering
Stephen C. Harvey, Ph.D., Georgia Research Alliance Professor, Georgia Institute of Technology
Joseph Bentz, Ph.D., Professor of Biology, Drexel University

AMYLOID FIBRIL NUCLEATION IN REVERSE MICELLES

This dissertation is dedicated to my parents, Fazilet and Zeki Eskici, in the hope that it may represent a validation of their sacrifices on my behalf.

ACKNOWLEDGMENT

It is customary for acknowledgment of dissertations to be a kind prose to express gratitude to many individuals. Given my sentimental personality and excellence of the individuals who deserve much more than one sentence of appreciation, I would like to present my deep gratitude to those beautiful people in a sincere way.

Dr. Paul H. Axelsen has been one of the greatest chances happened to me throughout my life. Being a faculty has been the dream of my life and the only reason for me to pursue a PhD degree. I will forever be indebted to Dr. Axelsen for helping me to make my dream come true. I thank him wholeheartedly, not only for his tremendous support, but also for giving me so many wonderful opportunities. He has generously invested his time and his patience in educating me. He has inspired me to become an independent researcher and helped me realize the power of critical reasoning. I also want to note that not many PhDs involve unforgettable fun moments, or special flight over Manhattan.

I have been fortunate to have Dr. Kim Sharp, Dr. Steve Harvey, Dr. Elizabeth Rhoades, and Dr. Ravi Radhakrishnan as my committee members. One of expected difficulties in graduate school life is arranging convenient times to have committee meetings (a.k.a. “herding cats”). They were available when I needed to reach them, and I always left our committee meetings encouraged. I am thankful to them for their concrete assistance, stimulating ideas and energy.

This study has brought a lot more than a doctoral degree. I feel very lucky to have met with Becky Axelsen, Anna Badkhen, Fyodor Badkhen, and Seçil Topaloğlu (a.k.a.

“my proton”). The moments I shared with these people helped me to continue and made life celebrated.

I owe special thanks to Shirley Yalman. Her involvement in the most defining moments of my life has been a true blessing. Her friendship and support of many years will always remain dear to my heart. She has been a role-model to me. I hope I can inspire my students as she has inspired me.

I am extremely grateful to have Lori Waselchuk, Shenid Bhayroo, Mira Bhayroo and Zahli Bhayroo in my life. They opened their warm home but most importantly their lovely hearts to me from the very first day of my life in US. They have been a second family to me, and it would be impossible to write these lines without their love and support. I thank them for the moments I remember with a smile and tears in my eyes.

Words cannot express all that I wish to say to my beloved parents and my wonderful sister, Fazilet-Zeki-Görkem Eskici. I deeply thank them for their unconditional trust, timely encouragement, and endless patience. It was their love that raised me up again when I got weary.

My deepest appreciation is to my husband, Haluk Özbay, who has redefined ‘patience’ and ‘love’, from 8194 kilometers away and 7 hours of time difference for the last five years.

Gözde Eskici

March 2017, Philadelphia

ABSTRACT

AMYLOID FIBRIL NUCLEATION IN REVERSE MICELLES

Gözde Eskici

Paul H. Axelsen

The 40-residue amyloid beta protein (Abeta) is the unstructured cleavage product of a common membrane protein that is produced in large quantities, but normally cleared from the brain before it exerts any apparent toxicity. Under some conditions, however, it undergoes a conformational change and aggregates into fibrils. These fibrils then coalesce into amyloid plaques, which are the pathognomonic brain lesions of Alzheimer's disease. The plaques are centers of active oxidative stress and neuronal death, so the conditions under which fibrils form is of high interest. When Abeta is encapsulated in a reverse micelle, its infrared spectrum indicates that it spontaneously adopts a fibril-like structure, which is remarkable because only one Abeta strand is present in each reverse micelle. That observation suggests that some aspect of the reverse micelle environment such as crowding, dehydration, proximity to a membrane, or high ionic strength may induce Abeta to nucleate amyloid fibril formation. Therefore, an understanding of the factors that induce Abeta to adopt fibril-like structure in reverse micelles may reveal what causes amyloid fibrils to form in Alzheimer's disease. Molecular dynamics simulations of Abeta in reverse micelles have been performed to identify and understand these factors. Results indicate that Abeta side chains penetrate the reverse micelle surface, anchoring the peptide in the membrane. Other interactions between peptide and membrane stabilize intrachain hydrogen bond formation and secondary structure. These interactions may be

important factors in the formation of amyloid fibrils and the pathogenesis of Alzheimer’s disease.

TABLE OF CONTENTS

LIST OF TABLES

LIST OF ILLUSTRATIONS

PREFACE

“I believe in evidence. I believe in observation, measurement, and reasoning, confirmed by independent observers. I'll believe anything, no matter how wild and ridiculous, if there is evidence for it. The wilder and more ridiculous something is, however, the firmer and more solid the evidence will have to be.”

— Isaac Asimov, The Roving Mind

Chapter 1: Introduction

Majority of “Reverse Micelle” section was originally published in Biochim Biophys Acta (Yeung, Eskici, & Axelsen, 2013) Priscilla S.-W. Yeung, Gözde Eskici and Paul H. Axelsen. Infrared spectroscopy of proteins in reverse micelles. *Biochim Biophys Acta*. 2013; 1828(10), pp 2314-2318. © 2017 Elsevier B.V.

1.1 - Background Information

The “cause” of Alzheimer’s disease remains largely unknown despite decades of increasingly intense study. Most cases have no genetic component and are variously called “sporadic”, “age-related”, or especially “late-onset” Alzheimer’s disease (**LOAD**). More than 5 million people currently have this disease, it is the 6th leading cause of death in the US, and there are no treatments available that alter its relentless course.

LOAD is characterized by an as-yet-undefined process occurring in the vicinity of amyloid plaques that causes neuronal dysfunction and death. These plaques consist largely of amyloid β (**Aβ**) peptides that, for unknown reasons, aggregate into fibrils and form amyloid plaques. No one knows whether fibrils/plaques are inherently neurotoxic, whether they arise with a neurotoxic “oligomeric” form of the Aβ peptide, or whether they represent the inert byproducts of a neurotoxic process. Nevertheless, fibril/plaque formation is such a consistent histopathological feature of LOAD that understanding the chemical mechanisms causing their formation in brain tissue is likely to explain why LOAD pathology develops in some individuals and not others, and at different ages among people who do develop the disease.

A key step in the pathogenesis of LOAD is the nucleation of Aβ fibril formation. When nucleation does not occur, Aβ peptides are rapidly cleared from the brain tissues where they are formed. When nucleation does occur, long-lived amyloid fibrils form, coalesce into plaques, and kill brain cells in their vicinity. Clearly, understanding the fibril nucleation event is a key to understanding the pathogenesis of LOAD.

Aβ fibrils have a characteristic in-register intermolecular parallel cross–β-sheet structure (Antzutkin et al., 2000), and it has been suggested that fibril nucleation is initiated by misfolded "seeds" (Kirkitadze, Condron, & Teplow, 2001; Terzi, Holzemann, & Seelig, 1997). These misfolded "seeds" are induced to form in extracellular spaces or subcellular compartments by macromolecular crowding (Minton, 2000). However, experimental characterization of these seeds is problematic as Aβ proteins spontaneously aggregate into fibrils at the concentrations required for many methods, and inhibiting their aggregation by cooling to 5 °C reveals only random coils (Hou et al., 2004). To circumvent these problems, Yeung and Axelsen have encapsulated the 40- residue Aβ protein (Aβ40) into reverse micelles and examined them with Fourier-transform infrared spectroscopy (FTIR). 40-residue Aβ protein (Aβ40) into reverse micelles and examined them with Fourier-transform infrared spectroscopy (FTIR) (Yeung & Axelsen, 2012).

FTIR revealed that monomeric Aβ proteins form a fibril-like structure in reverse micelles, while an analogue with a scrambled sequence does not. This observation suggests that some aspect of the reverse micelle environment such as crowding, dehydration, proximity to a membrane, or high ionic strength can induce Aβ to nucleate amyloid fibril formation. Therefore, an understanding of the factors that induce Aβ to adopt this conformation in reverse micelles may reveal how it is induced to form amyloid fibrils in Alzheimer's disease.

1.2 - Reverse Micelles

The dilute aqueous solution used in most *in vitro* studies presents remarkably different circumstances compared to *in vivo* circumstances (Luby-Phelps, 2000). In a cellular environment, many important biochemical reactions occur within confined aqueous microenvironments such as membranous organelles, extracellular spaces, and the interior of macromolecular chaperones. Moreover, cellular environment is considered as “crowded” because it contains high concentration of soluble macromolecules that occupy between 10 to 40% of the total fluid volume of the cell (Fulton, 1982; Zimmerman & Trach, 1991). High concentrations of dissolved macromolecules that alter the bulk properties of water, and lead to changes in the structure of proteins and the activity of enzymes (Chang, Liu, & Chen, 1994; Cringus et al., 2007; Faeder & Ladanyi, 2000; Fayer, 2011; Fragoso, Pacheco, & Karmali, 2012; Meersman, Dirix, Shipovskov, Klyachko, & Heremans, 2005; Moilanen, Fenn, Wong, & Fayer, 2009; Mukherjee, Chowdhury, & Gai, 2007). The effects of confinement and crowding may be mimicked in reverse micelles (RMs), making them useful models of biological microenvironments (Fayer, 2011).

RMs are spherical self-aggregates of amphiphilic surfactants that enclose nanometer-sized water droplets suspended in bulk organic solvent. The polar headgroups of the surfactant orient towards the water droplet, while the hydrophobic hydrocarbon chains orient away from the water and towards the organic solvent. Technically, the term “reverse micelle” is restricted to systems with low water content, but it is common to use the term for all spherical aggregates of surfactants in a predominantly organic media (Walde, MAO, Bru, Luisi, & Kuboi, 1992).

Confinement refers to the stable encapsulation of materials within the water droplet of an RM, while crowding refers to the exclusion of water from the vicinity of a molecule of interest by proteins, nucleic acids, or polysaccharides (Ellis & Minton, 2006; Zhou, 2008). The effects of confinement and crowding may be viewed as arising from two basic mechanisms. One is a reduction in the number of possible conformations for a polypeptide chain, which limits the entropy of its unfolded state, and reduces the entropic cost of folding (Zhou, 2008; Peterson, Anbalagan, Tommos, & Wand, 2004). Altered rates and paths for protein folding are typically attributed to this mechanism. The second mechanism is an alteration in the bulk properties of water due to the proximity of water molecules to a surfactant, an ion, or a macromolecule, and their involvement in a hydration shell. Changes in reaction rates and equilibria are generally attributed to this mechanism (Minton, 2001).

1.3 - Molecular Dynamics Simulations

Molecular systems are dynamic in nature, and analyzing their motions at the atomistic level is essential to understanding key physicochemical phenomena. Therefore, modeling the dynamic aspects of various systems has been of interest for decades in life science. In nature, these dynamics aspects are governed by quantum mechanical forces. In quantum mechanics, the Schrödinger equation takes the place of Newton’s equations. However, the Schrödinger equation is so complex that it can only be solved for very small systems. Direct numerical solution is limited to very small numbers of particles because the Schrödinger equation involves high-dimensional spaces. In order to understand dynamic aspects of larger systems, approximations are needed to simplify the problem. These approximations are often based on the Born-Oppenheimer assumption that separates the motion of nuclei and electrons. Thus, the Schrödinger equation, which describes the state of both electrons and nuclei, is separated into two coupled equations. Then, the motion of nuclei is defined according to the classical Newton's equations.

One of widely used method to understand dynamic aspects of larger systems is molecular dynamics (MD) simulations which is derived from the laws of quantum mechanics through stated approximations. In MD simulations, quantum mechanical forces are approximated by a sum of relatively simple equations—such as harmonic spring equations or Coulomb's equation. Therefore, instead of solving for quantum mechanics equations, MD simulations solve Newtonian mechanics equation and provide time averages of observables. One of the most fundamental axioms of statistical mechanics, "the ergodic hypothesis", states that the time average equals the ensemble average. The premise behind MD simulations is that if one system is simulated and evolved in time, that system will eventually pass through all possible states, and average of these representative states will provide experimentally relevant information concerning structural, dynamics and thermodynamic properties.

In a typical flowchart of MD simulation, starting point is to initialize the positions of and velocities of the atoms in the system. Forces for all molecules are calculated according to force field potential. Depending on chosen statistical ensemble, various thermostats and barostats can be used to control thermodynamic quantities. Once atoms move according calculated forces, all positions and velocities are updated. This loop continues until termination criteria are met.

In simulations of biomolecular systems, initial coordinates might be found in a protein data bank (PDB) file that contains the Cartesian coordinates (X, Y, Z) of every single atom in a protein, nucleic acid, or lipid. Each atom is given an initial velocity, and initial velocities satisfy a Maxwell-Boltzmann distribution at the desired temperature. Applied force field is a special case of energy functions, and refers to equations and parameter sets used to calculate the potential energy of a system. These parameters are derived from experiments to match with crystallographic, spectrographic, and quantum mechanical data.

A general form for the potential energy can be written as summation of bonded and non-bonded terms:

$$E(R) = E_{bonded} + E_{non-bonded}$$

where the energy E, is a function of the atomic positions, R, of all the atoms in the system (MacKerell, Jr. et al., 1998; MacKerell, Wiorkiewiczkuczera, & Karplus, 1995). The E_{bonded} term is sum of three terms:

$$E_{bonded} = E_{bond-stretch} + E_{angle-bend} + E_{rotate-along-bond}$$

These terms correspond to the three types of atom movement. The first term is a harmonic potential approximating the energy of bond-stretching vibrations between two atoms along a covalent bond that has ideal length, b_0:

$$E_{bond-stretch} = \sum_{1,2\ pairs} K_b(b - b_0)^2$$

where K_b is the force constant that determines the strength of the bond. Both b_0 and K_b depend on the chemical type of bonded atoms, and therefore, are parametrized to be specific to the type of bond and the elements involved.

The second term is a harmonic potential approximating the energy of bending vibrations in the angle that has ideal value of θ_0:

$$E_{angle-bend} = \sum_{angles} K_\theta (\theta - \theta_0)^2$$

where K_θ is harmonic force constant. Both θ_0 and K_θ depend on the chemical type of atoms constituting the angle, and therefore, are parameterized to be specific to the type of bond and the elements involved.

The third term is a torsional angle potential function that approximates the energetic barriers between two atoms separated by three covalent bonds, and corresponds to the rotation around the middle bond. This term is expressed as a cosine function:

$$E_{rotate-along-bond} = \sum_{1,4\ pairs} K_\phi (1 - \cos(n\phi))$$

where K_ϕ is the force constant belonging to the cosine type of potential and n is the coefficient of symmetry.

The energy term representing the contribution of non-bonded interactions in the potential function has two contributors, the Van der Waals (vdW) interaction energy and the electrostatic interaction energy (MacKerell, Jr. et al., 1998; MacKerell et al., 1995):

$$E_{non-bonded} = E_{van\ der\ Waals} + E_{electrostatic}$$

The vdW interaction is a result of a balance between repulsive and attractive forces between two atoms. While the attractive force (i.e. the dispersion force) arises from fluctuations in the charge distribution, the repulsive force arises where the electron-electron interaction is strong. Each of these two effects becomes negligible at infinite atomic separation and becomes significant as the distance between atoms decreases. At very short distances (less than the vdW radius), the repulsive interaction becomes dominant. This balance between repulsive and attractive forces results in a minimum in the energy. A Lennard-Jones 6-12 potential is usually used to model these VDW forces (MacKerell, Jr. et al., 1998; MacKerell et al., 1995):

$$E_{van\ der\ Waals} = \sum_{non-bonded\ pairs} \left(\frac{A_{ik}}{r_{ik}^{12}} - \frac{C_{ik}}{r_{ik}^{6}}\right)$$

where A_{ik} and C_{ik} are the atom-type dependent constants, and r_{ik} is the distance between two atoms. For faster calculations, a cutoff radius value is usually defined, and the energy of the Lennard-Jones potential is assumed to be zero at distances larger than cutoff value.

The electrostatic term of non-bonded energy approximates electrostatic interactions between two atoms, and it is modeled by a Coulomb potential:

$$E_{electrostatic} = \sum_{\substack{non-bonded \\ pairs}} \frac{q_i q_k}{D r_{ik}}$$

where D is the effective dielectric constant for the medium, and r_{ik} is the distance between two atoms having charges q_i and q_k.

The overall equation for potential energy can be written as:

$$E(R) = \sum_{1,2\ pairs} K_b(b - b_0)^2 + \sum_{angles} K_\theta(\theta - \theta_0)^2 + \sum_{1,4\ pairs} K_\phi(1 - \cos(n\phi)) + \sum_{non-bonded\ pairs}\left(\frac{A_{ik}}{r_{ik}^{12}} - \frac{C_{ik}}{r_{ik}^{6}}\right) + \sum_{\substack{non-bonded \\ pairs}} \frac{q_i q_k}{D r_{ik}}$$

Forces acting on atoms can be obtained as derivative of this potential energy function. Forces are calculated for all atoms in given time step and used to identify the velocities and positions of atoms in successive time step. Additional algorithms may be used to control fluctuations in thermodynamic properties.

A typical procedure to initialize a MD simulation includes (1) Defining initial positions, (2) solvating the system, (3) ionizing the system to neutralize overall charge, (4) minimizing the structure to eliminate bad contacts in the system, (5) equilibrating the system, (6) generating the trajectory (i.e. “production run”).

There are current limitations of MD simulations. First of all, force field parameters are approximations rather than accurate measurements. Therefore, results of MD simulations need to be validated with experiments. Second of all, reactions that involve the breaking or forming of covalent bonds cannot be modeled with MD simulations. Third of all, time scales of MD simulations are limited. Due to time limitation, important events may be missed, or the system may be trapped at trapped in a local minimum and obtained results would be biased.

In this study, the results of MD simulations were compared and validated with published experimental results. Moreover, MD simulations of this study were performed on specialized supercomputer to reach micro-second timescale.

1.3.1 - NAMD –Scalable Molecular Dynamics

NAMD is a parallel MD code and one of the most commonly used software designed for high-performance simulation of large biomolecular systems (Phillips et al., 2005). NAMD runs on various platforms ranging from super computers consisting of hundreds of processors to individual desktop and laptop computers. It can use the parameterizations from both CHARMM (MacKerell et al., 1998) and AMBER (Berendsen, Vanderspoel, & Vandrunen, 1995) force field specifications.

Periodic boundary conditions are introduced into MD simulations to eliminate surface effects at the boundary of the system. The unit cell that encloses all the particles of simulated system is replicated to infinity by periodic translations. This is done by replacing a particle leaving the cell from one side with a copy particle entering the cell on the opposite side (Phillips et al., 2005).

Computation of long-range non-bonded interactions is the bottleneck for MD codes, because the van der Waals and electrostatic interactions exist between every non-bonded pair of atoms in the system. NAMD performs this computation of long-range non-bonded interactions by spatially truncating interactions at a user-specified cutoff distance. When periodic boundary conditions are introduced, non-truncated electrostatic interactions can be computed by using particle-mesh Ewald (PME) method (Phillips et al., 2005).

The PME (Darden, York, & Pedersen, 1993) method is a fast numerical method to compute the Ewald sum, which is a description of the long-range electrostatic interactions for a spatially limited system with periodic boundary conditions. In this method, electrostatic interactions are calculated in two steps. While the short-range contribution is calculated in real space, the long-range contribution is calculated through reciprocal sum computed via fast Fourier transform (FFT) (Phillips et al., 2005).

NAMD uses the Verlet method for the integration and implements a multiple-time-stepping method to improve integration efficiency. While the shortest time step is 1 fs, time steps as long as 6 ps can be used along with “rigid bond” option (Phillips et al., 2005).

1.3.2 - Anton 1

Anton 1 is a special purpose supercomputer for MD simulations. This supercomputer is designed and built by D. E. Shaw Research in New York. The National Institutes of Health have supported an Anton for the biomedical research community at the Pittsburgh Computing Center, Carnegie-Mellon University.

Anton 1 comprised 512 application-specific integrated circuits (ASICs), and these ASICs were interconnected through a specialized high-performance network. The molecular system is decomposed spatially among these ASICs. Anton takes advantage of this MD specific hardware and parallelized algorithms that enhance scalability by reducing communication between and within chips (Shaw et al., 2008). Compared to high performance computing platform the Extreme Science and Engineering Discovery Environment (XSEDE), Anton 1 was 1000 times faster, and it was the only platform to reach microsecond timescale for all-atomistic simulations in a reasonable time.

While Anton does not have any running MD software, it uses a Desmond structure (DMS) file as an initial input and its trajectory output is compatible with Desmond’s (DTR files). It is compatible with CHARMM, AMBER and OPLS force fields.

For electrostatic interactions, Anton uses Gaussian split Ewald method (Shan, Klepeis, Eastwood, Dror, & Shaw, 2005). Similar to the PME method, electrostatic interactions are divided into two components. First component is computed directly for all pairs separated by less than cutoff radius. The second component is computed by taking the fast Fourier transform (FFT) of the mesh charges, multiplying by an appropriate function in Fourier space, performing an inverse FFT. Finally, resulting forces from mesh values are computed (Shan et al., 2005; Shaw et al., 2008).

Because output files of Anton 1 have large sizes and each user have limited memory, it is highly suggested to save coordinates at every 240 ps. Therefore, Anton 1 is ideal for the simulations of events happening over a long time scale.

1.3.3 - Anton 2

Anton 2 (Shaw et al., 2014) is a second-generation special-purpose supercomputer for MD simulations. Anton 2 has a better performance, capacity, and programmability than Anton 1. Current Anton 2 machine has 128 nodes, and it is ten times faster than its predecessor, Anton 1 (Shaw et al., 2014).

1.4 - Outline of the Thesis

In this thesis, MD simulations have been performed to determine the size of an RM, to elucidate how RM properties affect the conformation of amyloid beta, to study the effects of protein encapsulation on RM properties.

The following Chapter will explain approaches to determine the size of a protein-free RM, and will confront the first challenge, namely the creation of a reliable and efficient computational RM model. Experimentally, RM preparations are described by the molar ratio of water to surfactant, the water loading ratio (W_0). It is known that RM preparations for any given W_0 ratio have remarkably low polydispersity indices –the individual RMs are uniform in size. However, the W_0 value does not define the precise size of an RM for any given W_0 ratio. The challenge is compounded by wide discrepancies in the estimates of RM size and shape among experimental measurements, and between experimental and prior computational studies. RMs with W_0=7.5 of varying size have been created to examine their size, structure and shape. The number of surfactants per RM have been determined for W_0=7.5 from these simulations, and a balance of electrostatic forces is found to be primary factor determining RM size for a given W_0. An equation is provided to calculate the number of surfactant per RM for a wide range of W_0.

Chapter 3 examines RMs including Aβ peptides and provides detailed atomistic insight into previously published experimental observations about the remarkable behavior of Aβ40 peptides encapsulated in RMs. A competitive grant for Anton 1 was awarded to Eskici&Axelsen, and MD simulations of Chapter 3 were performed on Anton 1.

Chapter 4 examines mass exchange between RMs and the effect of peptide encapsulation on RM. This chapter will complement the results of Chapter 2. Because protein addition to RMs is likely to change protein-free RM properties. There are two possible models for encapsulation of protein: 1) protein replaces water and W_0 changes due to encapsulation; 2) Protein is added to RM without changing the number of components, therefore, the surface-area-to-volume ratio changes while W_0 is constant. While these models are tested, mass exchange between RMs of varying size will be examined. Another competitive grant for Anton 2 was awarded to Eskici&Axelsen, and MD simulations of Chapter 4 were performed on Anton 2.

Chapter 5 provides a summary of the work presented in this thesis as well as suggestions for future work that may be pursued.

Chapter 2: The Size of AOT Reverse Micelles

This research was originally published in the Journal of Physical Chemistry B (Eskici & Axelsen, 2016) Gözde Eskici and Paul H. Axelsen. The Size of AOT Reverse Micelles. *The Journal of Physical Chemistry B*. 2016; 120 (44), pp 11337–11347. ©American Chemical Society.

This work used the Extreme Science and Engineering Discovery Environment (XSEDE), which is supported by National Science Foundation grant number ACI-1053575. Primary research support was provided by GM76201 from the NIGMS.

I thank Dr. Kim Sharp and Dr. Stephen Harvey for valuable discussions.

2.1 - Overview

Reverse micelles (RMs) made from water and sodium bis(2-ethylhexyl) sulfosuccinate (AOT) are commonly studied experimentally as models of aqueous microenvironments. They are small enough for individual RMs to also be studied by molecular dynamics (MD) simulation, which yields detailed insight into their structure and properties. Although RM size is determined by the water loading ratio (i.e. the molar ratio of water to AOT), experimental measurements of RM size are imprecise and inconsistent, which is problematic when designing models for study by MD simulation. Therefore, a systematic study of RM size was performed by MD simulation with the aims of determining the size of an RM for a given water loading ratio, and of reconciling the results with experimental measurements. Results for a water loading ratio of 7.5 indicate that the interaction energy between AOT anions and other system components is at a minimum when there are 61-68 AOT anions in each RM. The minimum is due to a combination of attractive and repulsive electrostatic interactions that vary with RM size and the dielectric effect of available water. Overall, the results agree with a detailed analysis of previously published experimental data over a wide range of water loading ratios, and help reconcile seemingly discrepant experimental results. In addition, water loss and gain from an RM is observed and the mechanism of water exchange is outlined. This kind of RM model, which faithfully reproduces experimental results, is essential for reliable insights into the properties of RM-encapsulated materials.

2.2 - Introduction

Reverse micelles (RMs), composed of water and surfactant suspended in a nonpolar solvent, are popular experimental systems for the study of biological materials under conditions where they are physically confined with limited amounts of water. As such, they are models of crowded biological microenvironments such as membranous organelles, intercellular spaces, and the interior of macromolecular chaperones (Walde, Giuliani, Boicelli, & Luisi, 1990; Zhou, 2008; Yeung et al., 2013). While RMs can be made with diverse surfactant types, sodium bis(2-ethylhexyl) sulfosuccinate (aka aerosol OT or AOT) is popular because it readily forms RMs without a cosurfactant that are chemically stable, optically transparent, and capable of encapsulating relatively large amounts of water (Figure 2.1).

RM size in ternary AOT-based systems is determined by the water loading ratio (i.e. the mole ratio of water to surfactant, or W_0) (Vandijk, Joosten, Levine, & Bedeaux, 1989). Although the radius polydispersity (γ) of 0.065 - 0.30 reported for these systems (Ricka, Borkovec, & Hofmeier, 1991; Amararene et al., 2000; Kotlarchyk, Chen, & Huang, 1982; Kotlarchyk, Chen, Huang, & Kim, 1984; Robertus, Philipse, Joosten, & Levine, 1989; Farago, Richter, Huang, Safran, & Milner, 1990; Robinson, Toprakcioglu, Dore, & Chieux, 1984; Yan & Clarke, 1990) suggests that their size distributions are narrow, the absolute size of RMs is not a simple or direct measurement, and experimental estimates of AOT RM size vary by as much as 35% for any given W_0 value (Martinez et al., 2013). This uncertainty about RM size is problematic when performing molecular dynamics (MD) simulations for insight into the structure and organization of RMs because the number of molecular components in most simulations is fixed. The question of RM size remains unresolved despite numerous MD simulation studies with continuum solvent (Faeder & Ladanyi, 2000; Faeder & Ladanyi, 2001; Faeder & Ladanyi, 2005), coarse-grained surfactant (Brodskaya & Mudzhikova, 2006; Rosenfeld & Schmuttenmaer, 2011; Rosenfeld & Schmuttenmaer, 2006; Rodriguez, Marti, Guardia, & Laria, 2007; Pomata, Laria, Skaf, & Elola, 2008), and all-atom models (Abel, Sterpone, Bandyopadhyay, & Marchi, 2004; Martinez et al., 2013). For example, RM simulations of $W_0 = 7.5$ have been recently described with as few as 70 AOT molecules per RM (Chowdhary & Ladanyi, 2009), (n_{AOT}) and as many as 106 (Abel, Waks, & Marchi, 2010). One approach to answering the question of RM size via simulation has been to allow RMs to self-assemble from randomly distributed components. However, this approach is computationally expensive, and has thus far yielded systems with unexpectedly large indices of polydispersity (Marchi & Abel, 2015).

In this study, we address the question of RM size with MD simulations by examining the interaction energies within RMs across a range of sizes, and comparing the simulation results to previously published experimental data. The results of this horizontal study (at constant $W_0 = 7.5$) are also extrapolated vertically (across a range of W_0) to further test them against experimental data. When detailed attention is given to the nature of the experimental data, the insights provided by these simulations help reconcile many of the apparent discrepancies in available experimental data.

2.3 - Methods

2.3.1 - Simulations

Simulations were performed as NPT ensembles with NAMD 2.9 (Phillips et al., 2005), the CHARMM27 all atom force field for proteins and lipids (Foloppe & MacKerell, Jr., 2000), and TIP3P water (Jorgensen, Chandrasekhar, Madura, Impey, & Klein, 1983). Parameters for the AOT anion and isooctane (isoO) were obtained from previously published studies (Abel et al., 2004; Abel et al., 2010; Tian & Garcia, 2011a; Martinez, Malolepsza, Rivera, Lu, & Straub, 2014a). Long-range electrostatic forces were calculated with the Particle Mesh Ewald method (Darden et al., 1993) and an interaction cutoff of 12 Å was applied within periodic boundary conditions. Van der Waals (VdW) forces were smoothly shifted to zero between 10 Å and 12 Å. Equations of motion were integrated with the Verlet method and a time step of 2 fs. Langevin dynamics with a damping coefficient of 5 ps^{-1} was used to keep the temperature at 300 ºK. The pressure was maintained at 1 atm using a Nosé-Hoover-Langevin piston (Feller, Zhang, Pastor, & Brooks, 1995) .

Simulation systems were constructed by selecting a W_0 value and the number of surfactant molecules (n_{AOT}) to include in the system. These parameters determine the number of water molecules (n_{water}) to include, and the systems are denoted below as RM_X where $X = n_{AOT}$ and ranged from 34 to 106. A spherical cluster of $n_{water} + n_{AOT}$ water molecules was extracted from a well-equilibrated simulation of pure water at 300 ºK and 1 atm. AOT molecules were added by replacing n_{AOT} randomly selected water molecules with sodium cations, and distributing the anionic portions randomly on the surface of the cluster with SO_3 groups oriented inward. These water/AOT clusters were placed in the center of a truncated octahedron of sufficient size to contain 2536 molecules of isoO (n_{ISO}) – a number chosen so that the isoO mass was 83% of the total system mass for the largest RM and thus, within the RM-forming portion of the AOT/water/isoO phase diagram (Abel et al., 2010). Compositions of systems are listed in Table 2-1.

Simulation systems were equilibrated in four stages, each stage consisting of 0.01 ns minimization and 1 ns of NPT simulation. In stage one, all atoms except those in the isoO solvent were fixed in position. In stage two, the hydrocarbon tails of the AOT anions were unfixed. In stage three, the remaining portions of the AOT anions were unfixed. In stage four, all molecules in the system were unfixed. A separate simulation of a water droplet in isoO (without AOT) was equilibrated with only the latter two stages. Equilibrated systems were propagated for 30 ns with coordinates and energies saved every 0.001 ns. Only the final 15 ns of each trajectory were used for the data analysis. The entire process – system assembly, equilibration, and 30 ns simulation – was repeated twice for each system with a different water cluster and sodium cation substitutions to assess the reproducibility of results. A separate RM_{62} system was propagated for 100 ns to examine the time required for convergence (Towns et al., 2014).

2.3.2 - Analysis

Interaction energies for each saved coordinate set were calculated using VMD (Humphrey, Dalke, & Schulten, 1996) and the same parameters used to create the trajectory (VMD and NAMD therefore yield identical energies for the same structure). Four energies were calculated for individual members of each molecular species: its interaction with all other components of the same molecular species, and its overall interaction with each of the other three molecular species. These energies were averaged over all members of each species, and over all saved coordinate sets, for each simulation.

Most RMs quickly became ellipsoid in shape. Therefore, analysis of the distribution of components in terms of radial density profiles was problematic, and local nearest distance metrics were substituted in which the SO_3 groups demarcated the boundary between polar and apolar phases. The distance of various atoms and groups from this boundary surface was calculated (Fuglestad, Gupta, Wand, & Sharp, 2016). Each atom/group was assigned to a 1 Å layer, based on its distance to the nearest SO_3 headgroup. The thickness of the surfactant layer (r_{AOT}) is the distance from the boundary to the AOT terminal CH_3 groups, plus the radius of an SO_3 head group (3.1 Å) and the radius of a CH_3 group (2.3 Å). The various radii and distances referenced in this work are summarized in Table 2-2.

The radius of gyration (r_g) of simulated RM complexes was calculated as the root mean square distance between atom pairs according to equation 1:

$$r_g^2 = \frac{1}{2n^2}\sum_{i=1}^{n}\sum_{j=1}^{n}\langle(r_{ij})^2\rangle = \frac{1}{n}\sum_{i=1}^{n}\langle(r_{ic})^2\rangle \tag{1}$$

where n is the number of atoms, r_{ij} is the distance between atom i and j, and r_{ic} is the distance between atom i and the center of mass of the RM. To facilitate the comparison of r_g values from simulations with r_g values obtained from SAXS, only sodium, oxygen, and sulfur atoms were included in the calculation of r_g, because carbon and hydrogen atoms in AOT scatter X-rays to the same degree as the atoms in isoO, and do not create the electron contrast detected by SAXS.

RM shape was characterized by modeling the aqueous core consisting of water and sodium cations as an ellipsoid with the same mass and moments of inertia (Pomata et al., 2008; Brodskaya & Mudzhikova, 2006). The principal moments of inertia (I_1, I_2, and I_3) were calculated by determining the eigenvalues of the inertia tensor. For ellipsoids, the relations between semi-axes and principal moments of inertia are given by equations 2 – 4. The semi-axes a, b, and c of the ellipsoid systems were determined by solving equations 2-4 for a, b, and c:

$$I_1 = \frac{1}{5} m_{aq} (a^2 + b^2) \tag{2}$$

$$I_2 = \frac{1}{5} m_{aq} (a^2 + c^2) \tag{3}$$

$$I_3 = \frac{1}{5} m_{aq} (b^2 + c^2) \tag{4}$$

where m_{aq} is the combined mass of the water molecules and sodium cations. Because these calculations are based on the coordinates of atomic centers, and neglect the volume of the outermost water molecules, the VdW radius of a water oxygen ($r_O = 1.4$ Å) was added to each semi-axis, yielding a', b', and c'. Eccentricity, e, is a commonly used measure of the degree to which shape deviates from spherical (Abel et al., 2004; Chowdhary & Ladanyi, 2009; Vierros & Sammalkorpi, 2015). It was calculated from the semi-axes by

$$e = \sqrt{1 - \frac{c'^2}{a'^2}} \tag{5}$$

where e = 0 for a perfect sphere and approaches 1 for disc-like and rod-like shapes.

As RMs became ellipsoid, the hydrodynamic radius (r_h) of simulated RM complexes was determined according to equation 6:

$$r_h = (a'c'^2)^{1/3} + r_{AOT} \tag{6}$$

where r_h is equal to the radius of sphere that has the same volume as the ellipsoidal RMs (van Holde, Johnson, & Ho, 2006).

2.4 - Results

2.4.1 - Equilibration

The stability of system energy over time is a common criterion by which NPT simulations are judged to be suitably equilibrated. By this criterion, the water droplet and all 16 RM systems reached stable energies within 10 ns. However, simulated systems did not all reach a stable shape within this time, and some of the systems required nearly 15 ns to reach stable eccentricity values (Figure 2.2). Therefore, all simulations were run for 30 ns, but only the last 15 ns were deemed to be equilibrated and used for analysis.

2.4.2 - Energy analysis

The overall energy of each RM system varied with system size, so most energy terms were normalized by n_{AOT} to facilitate comparisons. Representative values for the various nonbonded interaction energies in the RM_{62} system are illustrated in Figure 2.3. The largest single term was the attractive electrostatic interaction between sodium cations and AOT anions. This attractive interaction was only partially balanced by repulsive interactions between cations and between anions. Relatively small negative energies were found for nonbonded isoO–isoO, AOT anion–isoO, water–AOT anion, water–sodium and water–water interactions.

Interaction energies involving AOT headgroups and sodium cations both become more positive with RM size, suggesting that these repulsive interactions favor smaller RMs at constant W_0 (Figures 2.4A,B). In contrast, interaction energies between sodium cations and AOT anions become more negative with RM size, suggesting that these attractive interactions favor larger RMs at constant W_0 (Figure 2.4C). Water-water and isoO-isoO interaction energies were -3 kcal/mol and -64 kcal/mol, respectively, and independent of system size (Figure 2.3). The interaction energies between AOT anions and isoO becomes slightly more positive with RM size (Figure 2.4D), while the interaction energies of water with sodium cations and with AOT anions exhibit no strong trend (Figure 2.4E).

The sum of the energies depicted in Figures 2.4A-E represent the energies of interaction between sodium AOT and all other system components. This “AOT energy” exhibits a minimum in the range of n_{AOT} = 62 to 68 (Figure 2.4F). However, the data from RM_{106} systems is anomalous. Together with the anomalous shape of this system (Figure 2.2, lower panel), it appears that they are unstable for reasons that are not reflected in the AOT energy. Fission into smaller systems appears imminent, and this behavior was not observed for any of the smaller systems. If the AOT energies in Figure

2.4F are fit while excluding the RM_{106} system, the minimum value corresponds to $n_{AOT} = 60.9$. This minimum may be related to a larger number of sodium cations in the immediate vicinity of AOT head groups (Figure 2.5). There is also a smaller number of water molecules in the immediate vicinity of AOT head groups (Figure 2.6), and in the immediate vicinity of sodium cations (Figure 2.7). To confirm that changes in AOT energy did not occur over longer times, the RM_{62} system was propagated for 100 ns (Figure 2.8). No systematic drift in AOT energy was detected beyond 10 ns.

Altogether, these results suggest that when $W_0 = 7.5$, RM with n_{AOT} of 61-68 are most stable, and that the structural basis for this stability is reduced screening of sodium cation – AOT anion interactions by water.

2.4.3 - RM Structure and Organization

Deviations from a spherical shape became larger with increased RM size, while fluctuations in eccentricity became smaller (Figure 2.2). If the size of an RM is not appropriate for a given W_0, shape distortion may occur because it is inherently unstable, without any indication of this distortion in the eccentricity value. For example, the RM_{106} system, illustrated in Figure 2.3, has a stable eccentricity value, but a highly distorted shape.

Nearest distance metrics indicate that water and sodium cations preferentially situate 2.5 Å closer to the center of the micelle than the SO_3 headgroups, but another layer of water and sodium cations situate 2.5 Å farther from the center than these groups (Figure 2.9). This pattern is a reflection of AOT anion penetration into the aqueous core of the RM, and displacement of water and sodium cations to the outside. It should be noted that an intermolecular distance of 2.5 Å is insufficient space for water molecules to situate between the ions. This observation, and the overall dominance of the interaction energy between sodium cations and AOT anions, is consistent with the aforementioned conclusion that RM stability is determined by the proximity of charged species and the extent to which water is available to screen the electrostatic interactions.

Figure 2.9 also shows that the distribution of isoO exhibits substantial overlap with the distribution of AOT chains, which is relevant to the observation in Figure 2.4D that interaction energies between AOT and isoO become more positive with RM size (discussed below). Finally, Figure 2.9 indicates that very few waters are more than 8Å inside of the SO_3 groups. It should be noted that this distance is not a useful measure of the aqueous core radius because the RM has an ellipsoidal shape, and because AOT headgroups penetrate into the aqueous core of the RM.

2.4.4 - Mass exchange

No loss or gain of sodium cations or AOT anions was observed over the course of the 30 ns simulations, but multiple water molecules both exited the RM into the isoO phase, and re-entered the RMs from the isoO phase. The number of water molecules gained and lost for all systems are listed in Table 2-3. There was no discernable difference in the first or second halves of the simulations, no apparent correlation between RM size and the rates of water gain/loss, and no tendency for a net change in n_{water}. In stark contrast, no molecules were lost from a pure water droplet in isoO over the same interval. This observation suggested that AOT anions were responsible for facilitating water transit in and out of the RM core. Although no attempt was made to estimate the magnitude of energy barrier that regulates water transfer, it was noted that the non-bonded interaction energy of a water molecule was -21 kcal/mol in the RM core, and -2.5 kcal/mol in the isoO phase. At various points in surfactant layer, the energy was approximately -10 kcal/mol. Thus, AOT anions appear to facilitate water transit in and out of the RM core by creating a population of water molecules at the interface with intermediate energies.

2.4.5 - Experimental correlation

A large number of experimental studies have been published that provide information about RM size. Some cannot be compared to the present results because they do not provide data for $W_0<12$. Some DLS results must be excluded because the AOT concentration ([AOT]) used was greater than 200 mM and such concentrations appear to distort the results of DLS experiments (Bohidar & Behboudnia, 2001). Since [AOT] = 140 mM in the simulations, only DLS studies performed with 100mM < [AOT] < 200 mM were compared (Bohidar & Behboudnia, 2001). However, there are 11 published studies of RM size that may be compared to the simulation results reported herein.

Amararene et al. (Amararene et al., 2000) reported SAXS results for RMs with W_0 values ranging from 3 to 30. Linear interpolation of their results for $W_0 = 7.5$ yields $r_g = 16 \pm 1$ Å. Yano et al. (Yano, Furedi-Milhofer, Wachtel, & Garti, 2000a; Yano, Furedi-Milhofer, Wachtel, & Garti, 2000b) reported SAXS results for RMs with W_0 values ranging from 3.5 to 24.4. Linear interpolation of their results for $W_0 = 7.5$ yields $r_g = 17 \pm 1$ Å. From the RM_{62} simulation and equation 2 we obtained $r_g = 15.7$ Å (Figure 2.10), in close agreement with both experimental results. SAXS measurements have also been reported by Hirai et al., who reported a sharp discontinuity in the relationship between r_g and W_0 at $W_0 = 10$. Linear interpolation of their results for $W_0 <$ 10 yields $r_g = 26$ Å for $W_0 = 7.5$ (Hirai et al., 1995), considerably larger than the other two aforementioned SAXS studies. However, a linear extrapolation of their results for W_0 > 10 yields $r_g = 18$ Å for $W_0 = 7.5$, which is in agreement with the other SAXS studies and with the simulation results reported herein.

When comparing SAXS and simulation results, it must be emphasized that conclusions about r_g are model dependent; whether the scattering entities are modeled as solid or hollow spheres has a significant influence on the results. A radial electron density profile for the RM_{62} system (Abel et al., 2004; Chowdhary & Ladanyi, 2009), approximated by weighting an ordinary radial density profile by atomic numbers, suggests that three regions with different X-ray scattering tendencies are present: an oxygen-rich region in the center, a transition region 10-15 Å from the RM center, and a relatively low density carbon-rich region beyond the transition region (Figure 2.9, upper panel). Some support for both solid and hollow models may be found in this graph, but the transition region – broadened as it is by eccentricity – suggests that nonspherical models must be considered for accurate results, and that simulations are needed to determine the n_{AOT} for an RM from an r_g measurement.

Eicke and Rehak reported LS measurements for RMs with W_0 values ranging from 2.78 to 44.44 and derived average apparent molecular weight estimates, from which values of n_{AOT} may be calculated. Exponential interpolation of their results for $W_0 = 7.5$ yields $n_{AOT} = 64$, which is in good agreement with the simulation results.

Numerous estimates of the hydrodynamic radius have been derived from experimental measurement of transport rates (Chatenay, Urbach, Nicot, Vacher, & Waks, 1987; Bohidar & Behboudnia, 2001; Vasquez, Williams, & Graeve, 2011; Kinugasa et al., 2002; Pal, Verma, Singh, & Sen, 2011; Nazario, Hatton, & Crespo, 1996; Zulauf & Eicke, 1979). Linear interpolations of these results for $W_0 = 7.5$ yield values for r_h ranging from 26 to 31 Å (Table 2-4). In some of these experimental studies, the thickness of AOT anion layer, r_{AOT}, was used to interconvert r_h and a "water pool radius" (Kinugasa et al., 2002; Amararene et al., 2000; Maitra, 1984). However, estimates of r_{AOT} used for this purpose ranged from 7 – 15 Å (Almgren, Johannsson, & Eriksson, 1993; Kotlarchyk et al., 1984; Amararene et al., 2000; Pal et al., 2011; Kinugasa et al., 2002; Zulauf & Eicke, 1979), and most were based on assumptions that the simulations show to be inaccurate (e.g. an extended conformation or a radial orientation for the aliphatic AOT chains). Nearest distance metrics (Figure 2.9) show that the density of CH_3 groups at the end of AOT (i.e. AOT terminal) anions is maximal 8.5 Å outside of the SO_3 groups. Therefore, the thickness of AOT anion layer appears to be 8.5 Å plus the radius of an SO_3 head group (~3.1 Å) and the radius of a CH_3 group (~2.3 Å), or $r_{AOT} \approx 13.9$ Å. To calculate r_h, the semi-axes a and c of the RM_{62} aqueous core were determined as 31.4, 14.5, and 12.3 Å respectively by solving equations 2-4 for a', b', and c'. Therefore, the simulations suggest that $r_h = 30.7$ Å (the sum of $(a'c'^2)^{1/3}$, ~16.8 Å and the r_{AOT}), which is within the range of published experimental values.

2.4.6 - Extrapolation to other values of W_0

The size of an RM "core" is here defined as the locus of points representing the centers of the AOT sulfonate head groups (r_{core}). This core would contain n_{water} water molecules, n_{AOT} sodium cations, and approximately half the volume of the n_{AOT} SO_3 groups. Assuming an overall density of ρ, the approximate volume of such a core is given by

$$V_{core} \cong \frac{n_{AOT}\left(W_0 m_{water} + m_{sodium} + m_{sulfate}/2\right)}{\rho} \qquad \text{(7-a)}$$

where m_{water}, m_{sodium}, and $m_{sulfonate}$ are the molar masses of water, sodium cations, and sulfonate anions, respectively. Given an average molecular volume for core components, $\bar{v}$, equation 7-a simplifies to

$$V_{core} \cong n_{AOT}\left(W_0 + \frac{3}{2}\right)\bar{v} = \frac{4}{3}\pi r_{core}^3 \qquad \text{(7-b)}$$

given the key assumption that the RM core is spherical in shape. The surface area of this core, A_{core}, is given by

$$A_{core} = a_{AOT} n_{AOT} = 4\pi r_{core}^2 \qquad \text{(7-c)}$$

where a_{AOT} is the surface area covered by an AOT anion, and its volume-to-surface-area ratio is given by

$$\frac{V_{core}}{A_{core}} = \frac{r_{core}}{3} = \bar{v}\,\frac{\left(W_0 + \frac{3}{2}\right)}{a_{AOT}} \qquad \text{(7-d)}$$

Equation 7-d illustrates the basis for a linear relationship between W_0 and r_{core}, and the use of linear extrapolations when calculating intermediate results in tabulated data. It follows that the number of AOT per RM is given by

$$n_{AOT} = \frac{4\pi r_{core}^2}{a_{AOT}} = 36\pi\left(W_0 + \frac{3}{2}\right)^2 \frac{\bar{v}^2}{a_{AOT}^3} \qquad \text{(7-e)}$$

Given $W_0 = 7.5$, $n_{AOT} = 62$ (from this study), and $\rho = 1.1$ g/cm^3 (estimated from 2014 Du et al) (Du, He, Yin, & Shen, 2014) equation 7-a yields $V_{core} = 18{,}414$ Å^3. Equation 7-b yields $\bar{v} = 33$ Å^3 per molecule, and $r_{core} = 16.4$ Å. Equation 7-c yields $a_{AOT} = 54.4$ Å^2, close to the published estimate of 55 Å^2.

A graph of n_{AOT} versus W_0 (equation 7-e, Figure 2.11, dotted line) compared to the published experimental data of Eicke and Rehak (red dots) (Eicke & Rehak, 1976) and of Amararene et al. (blue diamonds) (Amararene et al., 2000) shows that agreement away from $W_0 = 7.5$ is poor. In particular, equation 7-e fails to predict the experimentally observed value of $n_{AOT} = 15$ for $W_0 = 0$, and it overestimates n_{AOT} by 37% for $W_0 = 45$. This discrepancy suggests that a "dry" term must be added to equation 7-e in the form of $n_{AOT}^0 = 13.6$ to correct for the number of AOT molecules in a water-free RM. With that correction, and an increase in a_{AOT} to 59.1 Å^2, equation 7-f agrees with the entire range of results from Eicke and Rehak, and the results of Amararene et al. beyond $W_0 = 15$ (Figure 2.11, solid line).

$$n_{AOT} = 36\pi\left(W_0 + \frac{3}{2}\right)^2 \frac{\bar{v}^2}{a_{AOT}^3} + n_{AOT}^0 \qquad \text{(7-f)}$$

RM preparations may be characterized experimentally by a radius polydispersity index (γ), and reported values range from 0.065 to 0.30 (Ricka et al., 1991; Amararene et al., 2000; Kotlarchyk et al., 1982; Kotlarchyk et al., 1984; Robertus et al., 1989; Farago et al., 1990; Robinson et al., 1984; Yan & Clarke, 1990), although only the value of $\gamma =$

0.15 from Amararene et al. was measured in isoO (Amararene et al., 2000). This index may be converted into a standard deviation for the distribution of radii using equation 8:

$$\gamma^2 = \frac{\langle {r_{core}}^2 \rangle - \langle r_{core} \rangle^2}{\langle {r_{core}}^2 \rangle} = \frac{\sigma^2}{\langle {r_g}^2 \rangle} \quad or \quad \sigma^2 = \frac{\gamma^2 \langle r_{core} \rangle^2}{1 - \gamma^2} \qquad (8)$$

where σ is the standard deviation of r_{core}. Assuming that $\gamma = 0.15$, equation 8 suggests that $\sigma = 2.5$ Å for r_{core}, while equation 7-f suggests that n_{AOT} ranges from 43 to 79 for RMs with $r_{core} = 16.6 \pm 2.5$ Å.

2.5 - Discussion

The chief result of this investigation is a quantitative understanding of the relationship between W_0 and the size of a RM in the commonly used water/AOT/isooctane system. It has long been appreciated that there is a linear relationship between W_0 and RM radius, justified largely in geometric terms (as per eq. 7-d) above. However, widely divergent slopes have been proposed for this relationship, and it is not immediately clear how to infer the number of AOT molecules in an RM from the radius information that such slopes provide. The results in this study suggest that RMs with a $W_0 = 7.5$ most likely contain between 61-68 AOT molecules per RM, with a second moment distribution of radii that correspond to n_{AOT} from 43 to 79 (calculated using equation 8). From this benchmark, n_{AOT} for W_0 ranging from 0 to 45 may be predicted from equation 7-f in excellent agreement with experimental results.

There are several other important results from this study. One is a physicochemical explanation for the relationship between W_0 and n_{AOT}, and for the expectation that each value of W_0 has a value of n_{AOT} where the AOT energy is a minimum. The AOT energy has three main components: (1) the electrostatic attraction between sodium cations and anionic AOT head groups, (2) the electrostatic repulsion between anionic AOT head groups, and (3) the electrostatic repulsion between sodium cations (Figure 2.5). The fits to the data in Figures 2.4A-D help clarify trends in the noisy data, such as the tendency for repulsive interactions to favor smaller RMs, and for attractive interactions to favor larger RMs at constant W_0. The size of an RM appears to be determined primarily by a balance between these attractive and repulsive interactions, and the availability of water to screen them. To some extent, the interaction energies between the AOT anion and isoO also favor smaller RMs at constant W_0. These energies are primarily due to VdW interactions, which may increase in magnitude in smaller RMs because curvature – and hence, the wedge-shaped gaps in the AOT layer into which isoO may penetrate – is greater in smaller RMs.

A third important result from this study is the ability to reconcile experimental results that are reported in units that are difficult to interconvert, such as radius-of-gyration, hydrodynamic radius, and aggregation number. Widely discrepant experimental results have been noted for some time (Abel et al., 2004; Martinez et al., 2013; Marchi & Abel, 2015), but upon close examination some of these discrepancies may be attributed to differences in solvents (Kinugasa et al., 2002) or temperature (Marchi & Abel, 2015). Other discrepancies are due to linear interpolation between n_{AOT} vs W_0 when a nonlinear interpolation is needed, or to a comparison of r_g and r_{core} without suitable conversion (Martinez et al., 2013). Most of the remaining studies may be reconciled by a well-informed estimation of the surfactant layer thickness. The value of $r_{AOT} \approx 13.9$ Å suggested by the simulations helps reconcile published values with each other and revise previously calculated values for r_{core}. In general, simulations are essential for interpreting experimentally derived values such as r_g and r_h in terms of the n_{AOT} for an RM.

A fourth important result is insight into the shape and internal organization of an RM. Deviations from spherical shape observed in these simulations are significant to an understanding of RM size and other characteristics observed in experimental studies. For example, the simulations show that the distributions of water and AOT overlap to a large extent, so that n_{AOT} and hence, the size of an RM in terms of the number of its component molecules, is not easily derived from any of the experimentally derived radii defined in Table 2-2.

A fifth important result is insight into the mechanism of water exchange between RMs. Intermicellar exchange has been demonstrated experimentally, but has not been reported in previous all-atom RM simulations (Marchi & Abel, 2015; Abel et al., 2004; Chowdhary & Ladanyi, 2009; Vasquez et al., 2011; Abel et al., 2010). It has been suggested that the mechanism of intermicellar water exchange involves sequential fusion and fission of RMs (Fletcher, Howe, & Robinson, 1987), or channels forming during micellar collisions (Jada, LANG, & Zana, 1989; Howe, Mcdonald, & Robinson, 1987). However, the simulations demonstrate that the AOT anion facilitates the loss and gain of individual water molecules from an RM, most likely by creating a population of water molecules with an energy that is intermediate between the aqueous and isooctane phases.

This population is evident from the nearest distance metrics which show extensive overlap of the water, AOT anion, and isoO distributions (Figure 2.9).

It should be noted that the simulations in this study were performed nominally at 300K, but they are being compared to experimental studies at 293 or 298K. While it would have been a simple matter to adjust the simulation temperature to the temperatures of the experiments, the simulation parameters have been optimized for 300K. There is no simple way to adjust a parameter set so that is valid at other temperatures. More importantly, perhaps, there may be no need to make this adjustment because experimentally determined r_h values did not change over temperatures ranging from 288°K to 318°K (Zulauf & Eicke, 1979; Nazario et al., 1996). The accuracy of common parameter sets has also been questioned because of the high concentrations found in RM systems (Goh, Eike, Murch, & Brooks, 2015), although the reported inaccuracies were manifest in properties not examined in this study.

Finally, this study provides a starting point for the accurate simulation of materials encapsulated in RMs. There are significant differences in the interpretation of RM properties, with or without protein inside, in the literature. Although many experimental studies are interpreted with the assumption of an idealized spherical geometry of the RM, most computational studies support the conclusion that encapsulated materials do not experience the conditions of a hard spherical confinement (Abel et al., 2010; Martinez et al., 2014a). Moreover, encapsulated material will likely increase the volume and surface area of an RM. The need for extra surfactant to cover the increased surface area may be met by (1) the coalescence of RMs with same W_0 ratio, which would result in a larger RM with same W_0 ratio (2) the acquisition of surfactant from other RMs, which would result in a smaller W_0, (3) the replacement of water with the encapsulated material, which would negate the need for additional surfactant but result in a smaller W_0, or (4) situating portions of the encapsulated material at the interface to substitute for surfactant. In any of these possibilities, the AOT energy would be determined by not only by electrostatic interactions between surfactant, sodium cations, and water but also by the physicochemical characteristics of the encapsulated material. Simulation studies of encapsulation are needed to explore these possibilities.

2.6 - Conclusion

An RM with $W_0 = 7.5$ appears to be most stable when $n_{AOT} = 61 - 68$, and this relationship is determined by a balance of electrostatic forces that are modulated by the dielectric effect of encapsulated water. From this benchmark value, n_{AOT} may be calculated for a wide range of W_0 values in close agreement with experimental data. The information obtained from simulations about RM structure and organization enables helps reconcile many of the seemingly inconsistent experimental results about RM size.

Table 2.1 - Compositions of simulated systems*

System	$\boldsymbol{n_{AOT}}$	$\boldsymbol{n_{water}}$	$\boldsymbol{n_{atoms}}$	$\boldsymbol{f_{iso}}$(%)	$\boldsymbol{r_W}$ (Å)	$\boldsymbol{s}$ (Å)
WD	-	255	66701	98	12.3	95
RM_{34}	34	255	68945	94	12.3	98
RM_{46}	46	345	70007	92	13.6	98.5
RM_{50}	50	375	70361	91	13.9	98.7
RM_{54}	54	405	70715	90	14.4	98.9
RM_{58}	58	435	71069	90	14.8	99
RM_{60}	60	450	71246	89	14.9	99.1
RM_{62}	62	465	71423	89	15.1	99.2
RM_{64}	64	480	71600	89	15.3	99.3
RM_{66}	66	495	71777	88	15.4	99.4
RM_{68}	68	510	71954	88	15.6	99.5
RM_{70}	70	525	72131	88	15.7	99.6
RM_{74}	74	555	72485	87	16.1	99.7
RM_{78}	78	585	72839	87	16.4	99.8
RM_{82}	82	615	73193	86	16.7	100
RM_{94}	94	705	74255	84	17.4	100.4
RM_{106}	106	795	75317	83	18.2	100.9

* n_{AOT} and n_{water} are the numbers of AOT and water molecules. n_{atoms} is the total number of atoms in each system. f_{iso} is the mass fraction of isoO as a percentage of mass of all components in the system. r_W is the average distance from the center of the RM to the outermost water molecule. s is edge length of the truncated octahedron unit cell.

Table 2.2 - Radius definitions

Symbol	**Definition**
r_W	Average distance from the center of the RM to the outermost water molecule (used only in Table 2-1)
r_h	Hydrodynamic radius of RM complexes
r_{AOT}	Thickness of the surfactant shell
r_g	Radius of gyration of RM complexes
r_0	VdW radius of a water oxygen
r_{core}	Radius of the core containing water, sodium cations, and approximately half the volume of SO_3 groups

Table 2.3 - Water losses and gains for simulated RM systems*

System	Loss	Gain	Net
WD	0	0	-
RM_{34}	7	6	-1
RM_{46}	5	5	0
RM_{50}	6	5	-1
RM_{54}	7	4	-3
RM_{58}	7	7	0
RM_{60}	6	6	0
RM_{62}	8	7	-1
RM_{64}	7	5	-2
RM_{66}	6	6	0
RM_{68}	11	11	0
RM_{70}	9	7	-2
RM_{74}	6	6	0
RM_{78}	7	7	0
RM_{82}	12	11	-1
RM_{94}	8	7	-1
RM_{106}	8	7	-1

**counts are for the entire 30-ns simulations*

Table 2.4 - Interpolated values of r_h for W_0=7.5 from published experimental studies and the value of r_h from the RM_{62} simulations.*

r_h (Å)	Technique	Reference
26	FRAPP	Chatenay et al.(Chatenay et al., 1987)
27	DLS	Bohidar and Behboudnia(Bohidar & Behboudnia, 2001)
28	DLS	Vasquez et al.(Vasquez et al., 2011)
31	Viscosity measurements	Kinugasa et al.(Kinugasa et al., 2002)**
29	FCS	Pal et al.(Pal et al., 2011)
30	DLS	Nazario et al.(Nazario et al., 1996)
31	PCS	Zulauf and Eicke(Zulauf & Eicke, 1979)
30	MD simulations	Eskici and Axelsen

*DLS – dynamic light scattering. FRAPP – fluorescence recovery after fringe pattern photobleaching. FCS – fluorescence correlation spectroscopy. PCS – photon correlation spectroscopy. ** r_h was estimated from Kinugasa et al.(Kinugasa et al., 2002) by assuming $r_{AOT} = 13.9$ Å.

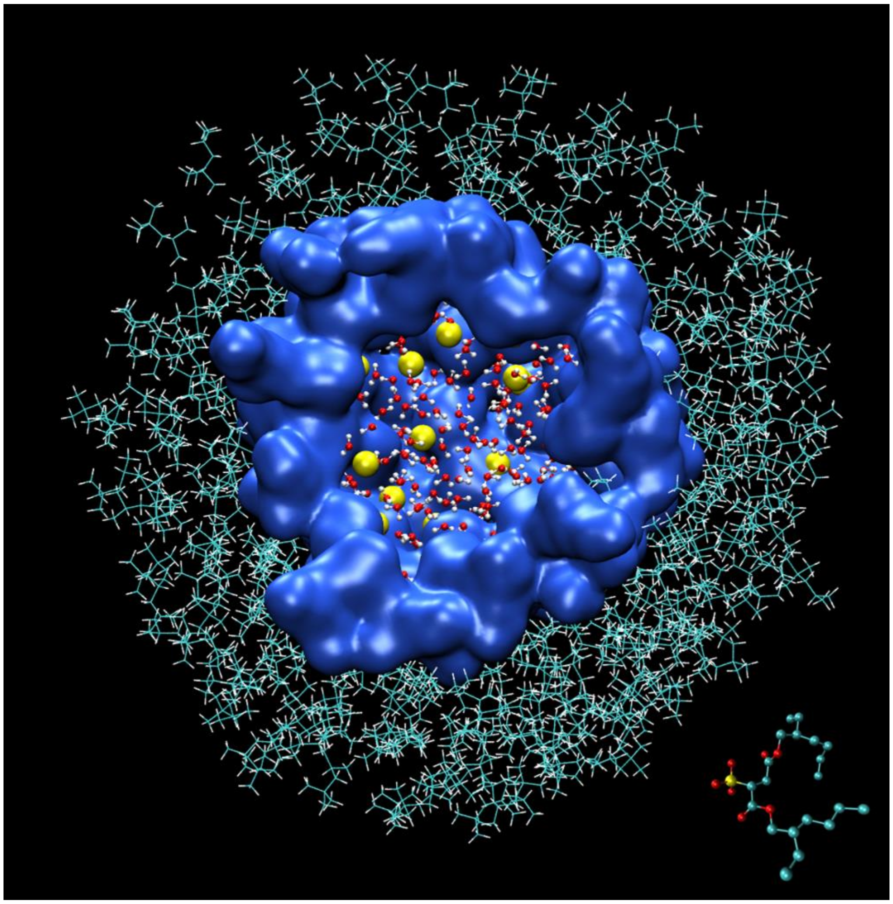

Figure 2.1 - Cross section of an RM model with W_0 = 7.5 and 62 AOT.
Water molecules are rendered as CPK models, sodium cations as yellow van der Waals spheres with a radius of 0.6 Å, AOT anions as a blue surface, and isooctane as lines. A single AOT anion is rendered as a CPK model in the lower right corner.

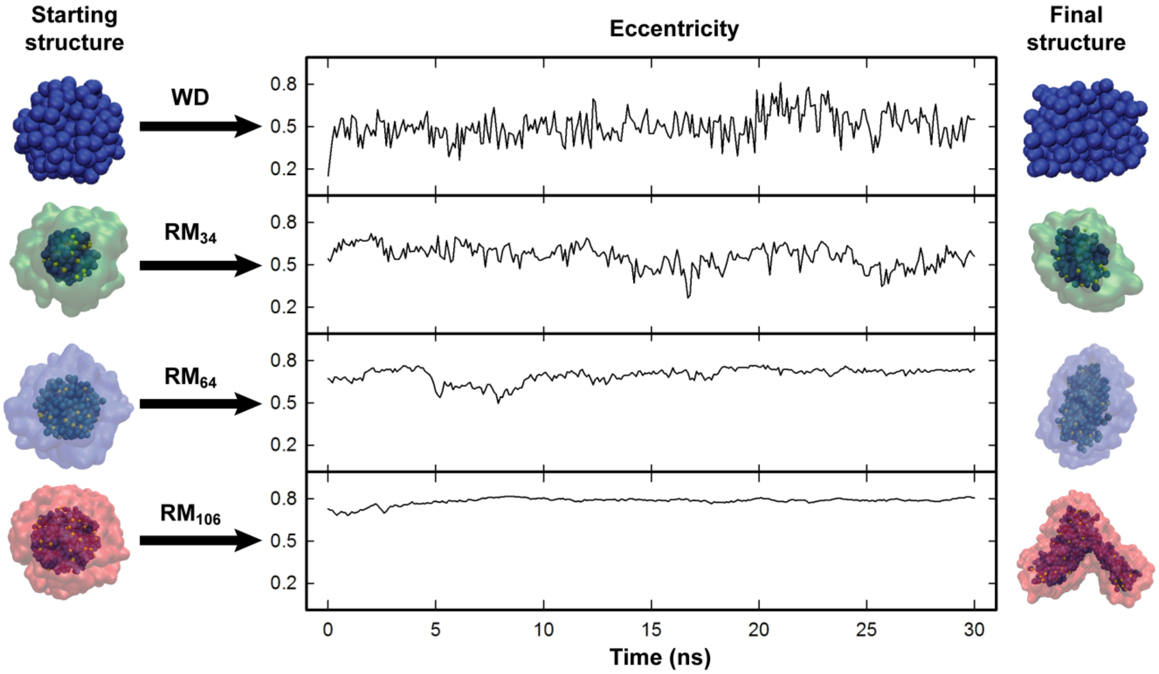

Figure 2.2 - Eccentricity vs time for the WD, RM_{34}, RM_{64}, and RM_{106} systems.

On either end of each graph, the initial and final structures are illustrated by representing water molecules as blue spheres, sodium cations as yellow spheres, and AOT anions as a surface. The starting structures were energy minimized before marking time “0” in the eccentricity graphs. Note that the final structure of the RM_{106} system is highly distorted. This degree of distortion was not reflected in the eccentricity calculations; fission into smaller systems appeared imminent. There were no shape distortions suggesting imminent fission observed in any of the smaller systems.

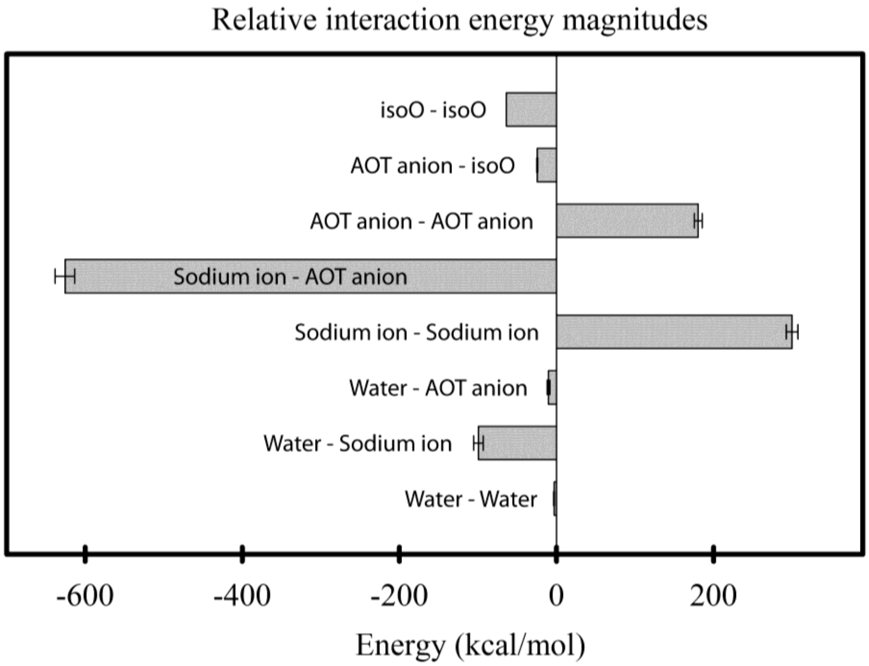

Figure 2.3 - Relative magnitudes of all pairwise nonbonded interaction energies for an RM$_{62}$ system, normalized by n$_{AOT}$.

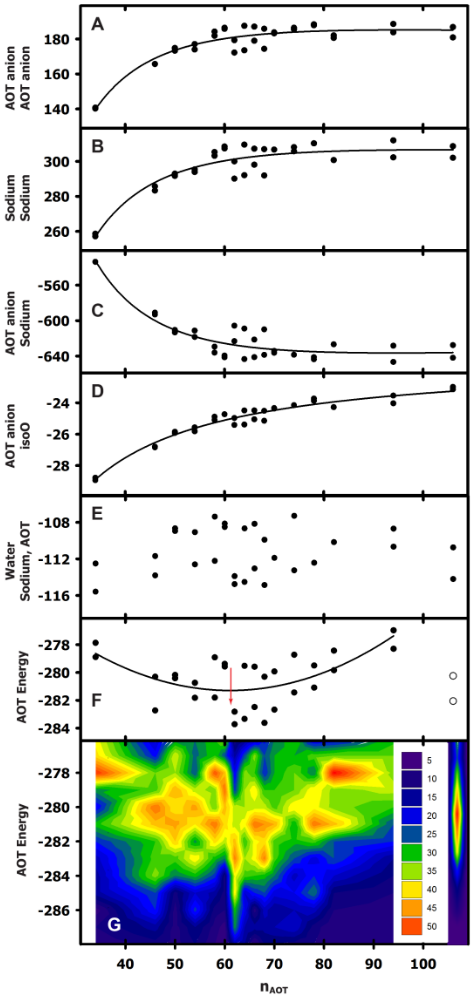

Figure 2.4 - RM system nonbonded interaction energies in kcal/mol normalized by n_{AOT}.

(A) AOT anion−AOT anion interaction energies with an inverse second order fit. (B) Sodium cation−sodium cation interaction energies with an inverse second order fit. (C) AOT anion−sodium cation interaction energies with an inverse second order fit. (D) AOT anion−isoO interaction energies with an inverse second order fit. (E) The sum of water−AOT anion and water−sodium cation interaction energies. There are two results for each system in panels A−E from the two independent 30 ns simulations, that sometimes superimpose. (F) AOT energy (defined in the text, i.e., the sum of the energies depicted in panels A−E) with a quadratic fit to all data except the RM_{106} system (indicated in open circles). The value of n_{AOT} at the minimum is 60.9 (vertical red arrow). (G) Histograms of the AOT energies combined into a contour graph. Autocorrelation times for the AOT energies were generally less than 100 ps. Therefore, energies were calculated at 100 ps intervals for the two 15 ps simulations for each system, divided into 1 kcal/mol bins, and color-coded according to bin counts as indicated.

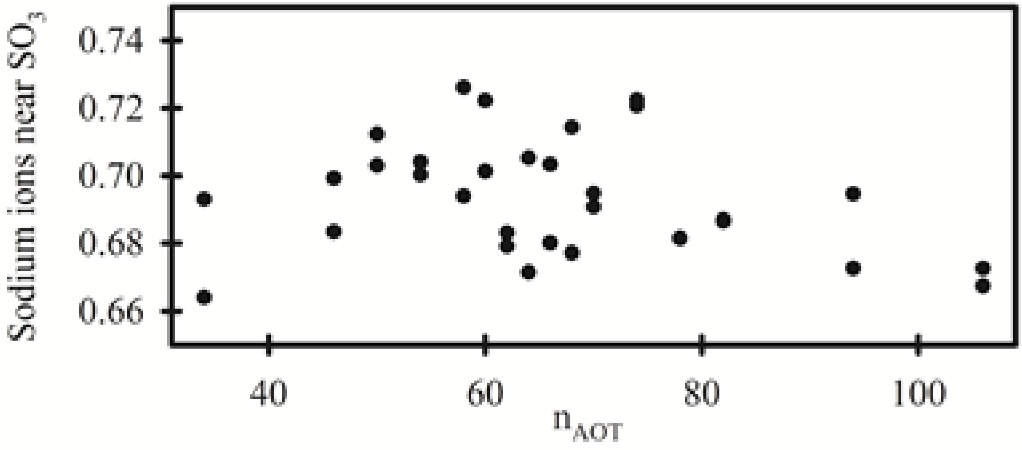

Figure 2.5 - Average number of sodium cations within 3 Å of the SO_3 groups. The two results for each value of n_{AOT} were derived from the two independent 30 ns simulations.

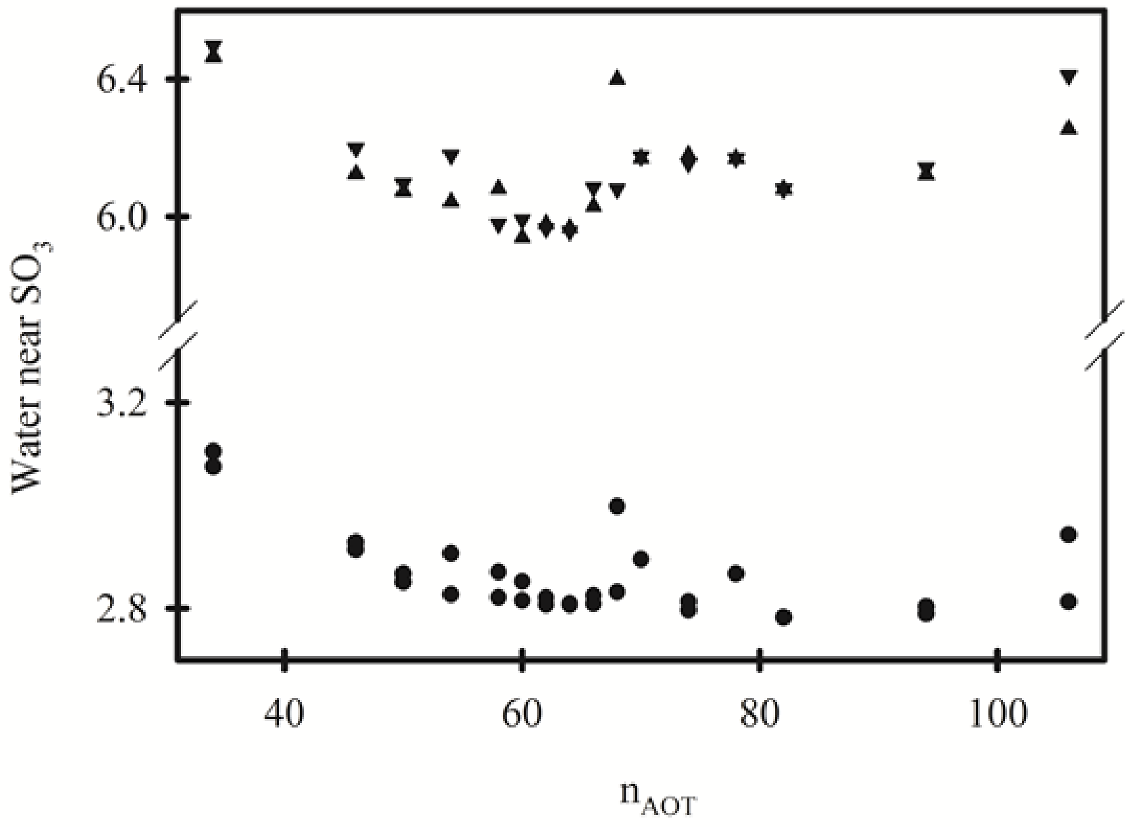

Figure 2.6 - Average number of water molecules within 3 Å (circles) and 5 Å (triangles) of the SO_3^- groups.
The two results for each value of n_{AOT} were derived from the two independent 30 ns simulations.

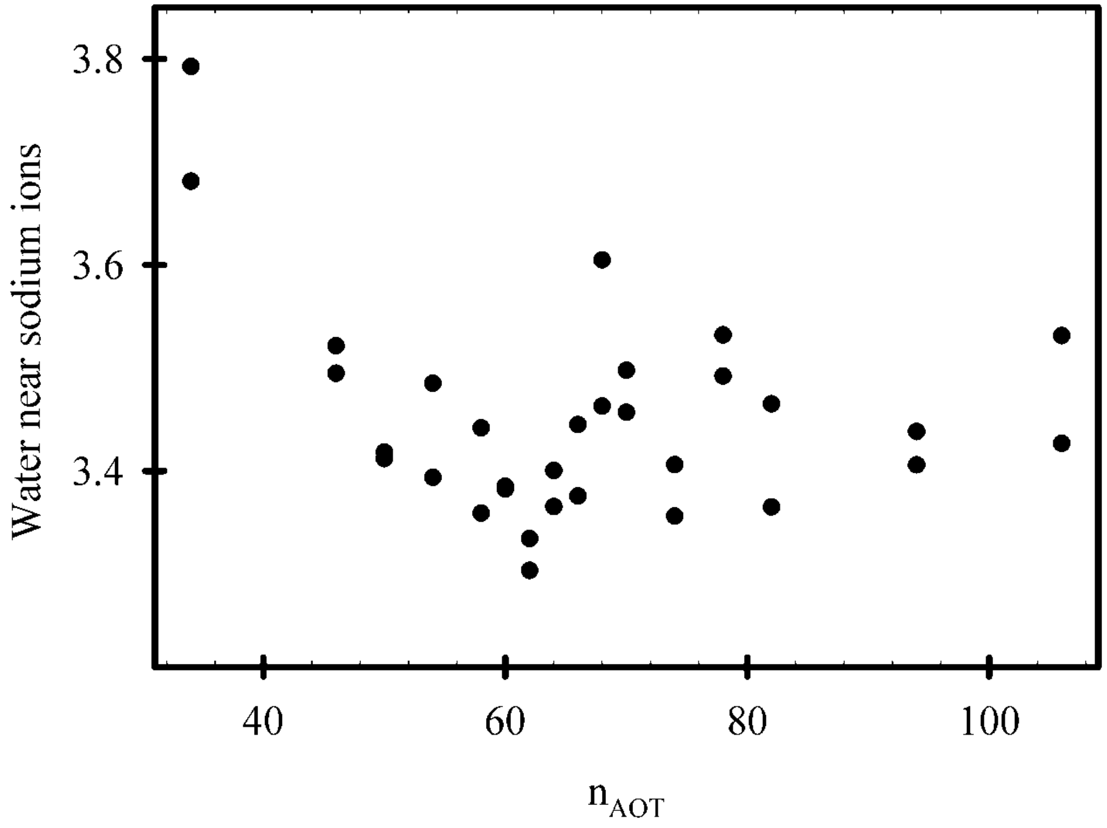

Figure 2.7 - Average number of water molecules within 3 Å of sodium cations. The two results for each value of n_{AOT} were derived from the two independent 30 ns simulations.

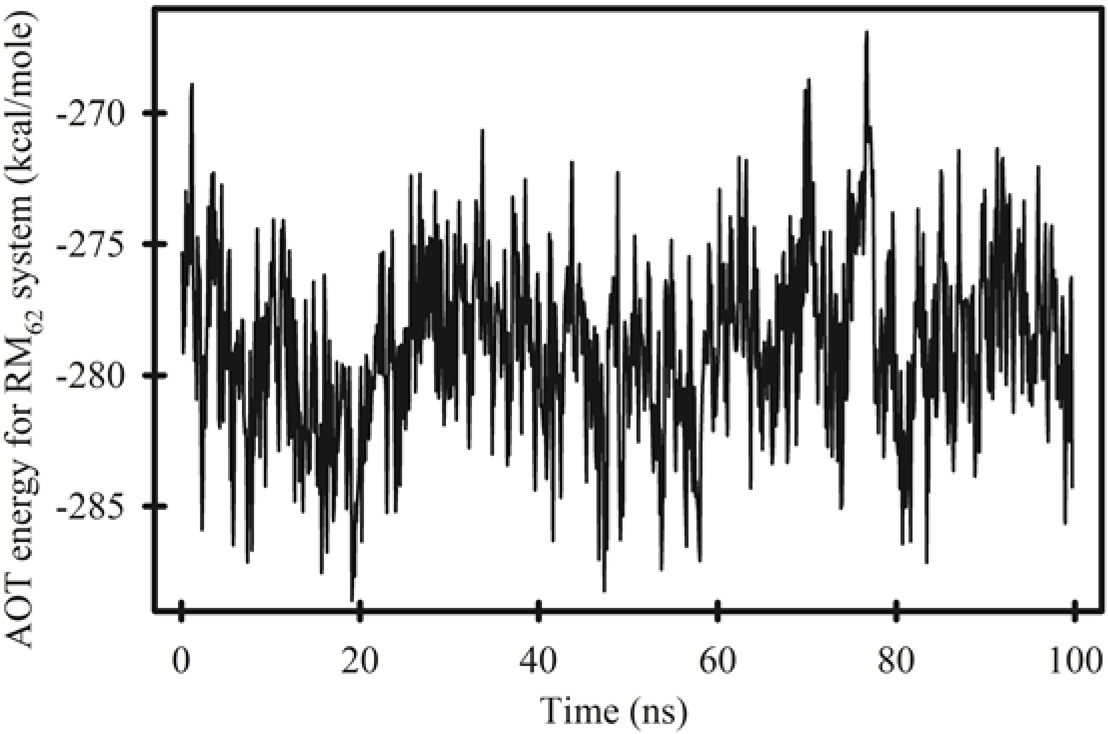

Figure 2.8 - AOT energies over 100 ns for an RM$_{62}$ system.

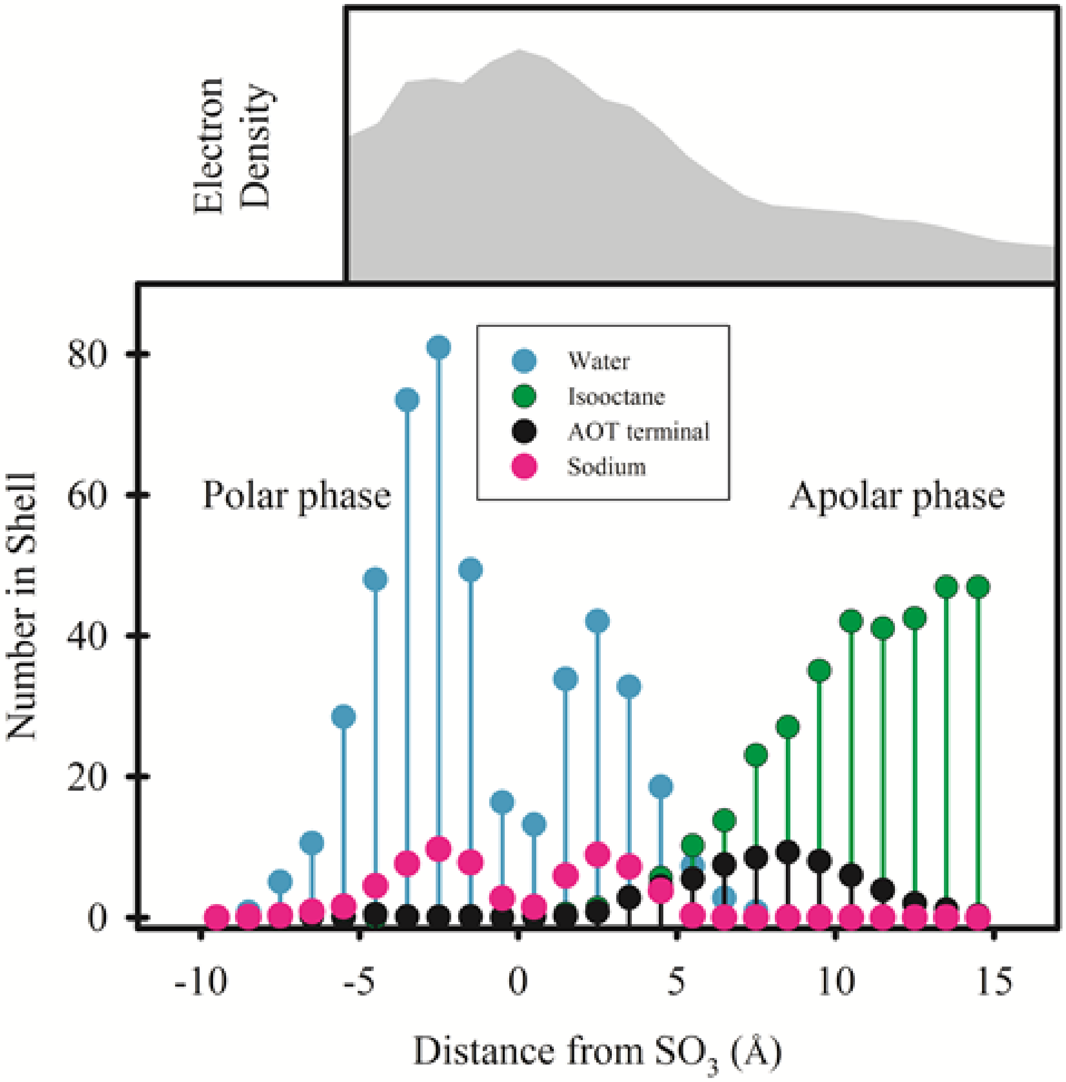

Figure 2.9 - Distribution of components in an RM_{62} system.
Lower panel: Nearest distance metrics analysis (Fuglestad et al., 2016) with distance to the nearest SO_3 group on the horizontal axis. The polar phase is comprised primarily of water (blue) and sodium cations (magenta). The apolar phase is comprised of AOT chains (black) and isoO (green). The AOT terminal methyl groups are indicated to enable the determination of $\boldsymbol{r_{AOT}}$ as described in the text. Upper panel: a radial electron density profile approximated by weighting an ordinary radial density profile by atomic numbers. The horizontal axis is roughly aligned with the distance scale of the lower panel. The vertical axis is arbitrary.

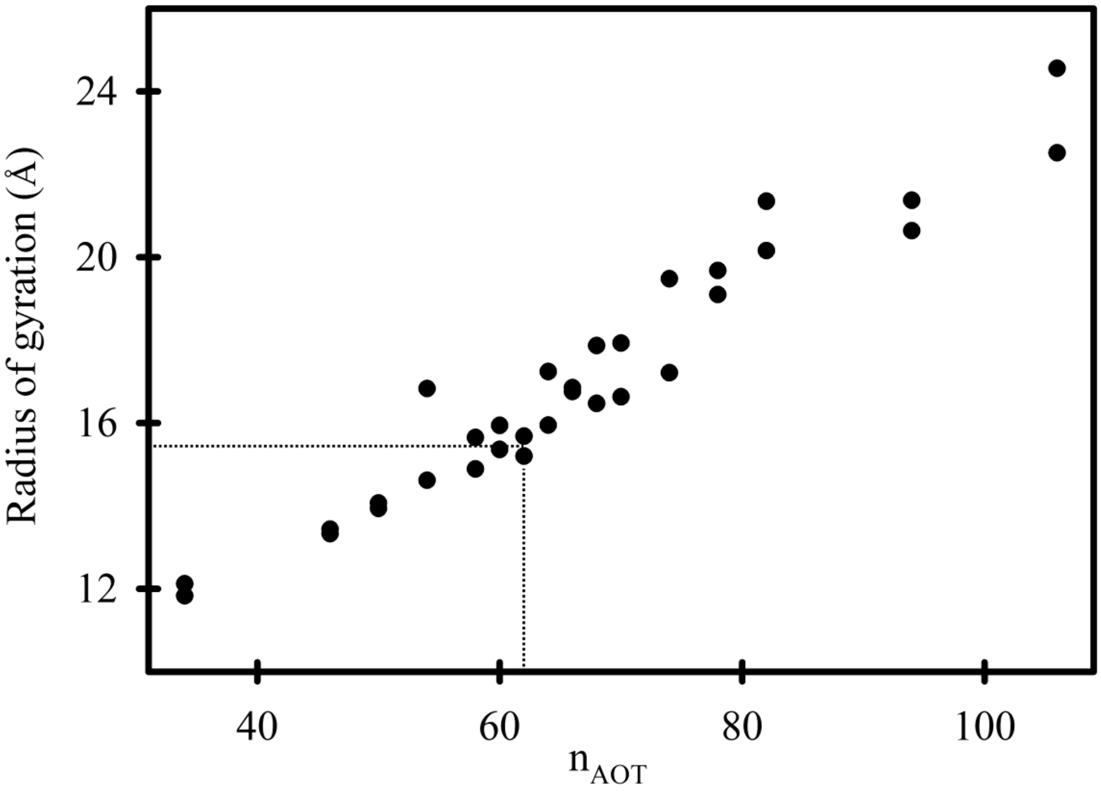

Figure 2.10 - Radius of gyration vs n_{AOT} for simulated RM systems.
The two results for each value of $\boldsymbol{n_{AOT}}$ were derived from the two independent 30 ns simulations. The average radius of gyration for the RM_{62} system is 15.7 Å, and indicated with dotted lines.

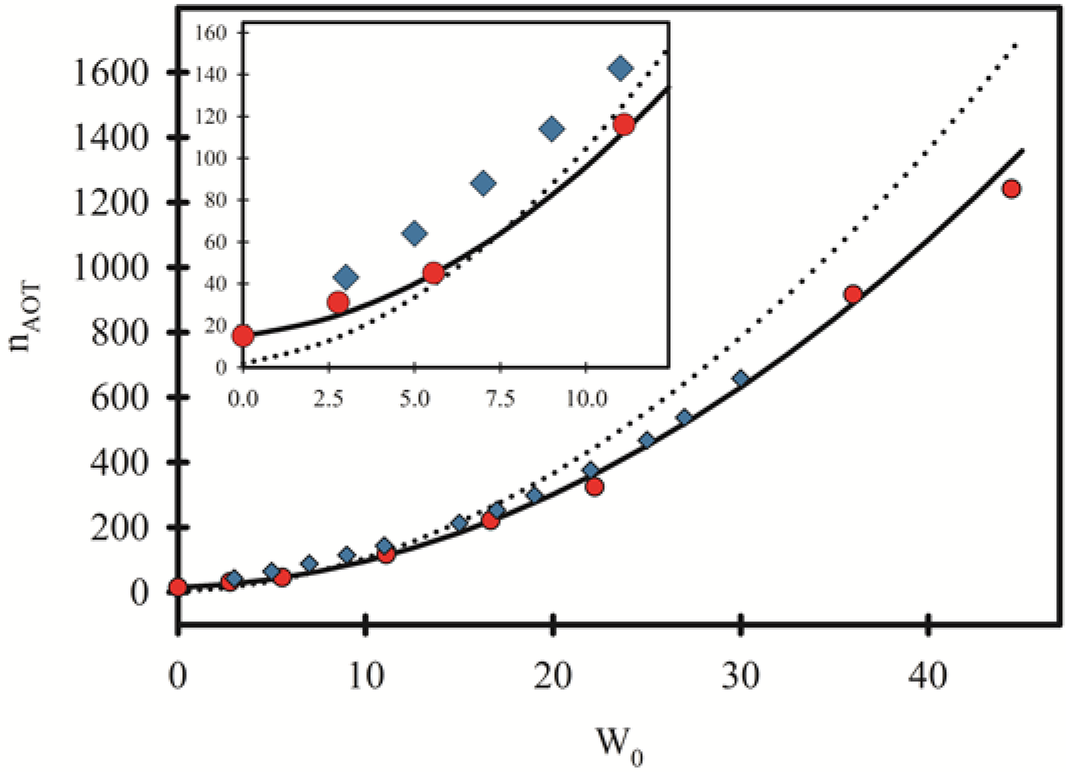

Figure 2.11 - Extrapolated results for various W_0 and comparison with experimental studies.

Solid line – n_{AOT} values obtained from equation 7-f which include the n^0_{AOT} "dry" term and a slightly larger value of a_{AOT}. Dotted line – n_{AOT} values obtained from equation 7-e. Red circles – the published experimental data of Eicke and Rehak(Eicke & Rehak, 1976). Blue diamonds – the published experimental results of Amararene et al (Amararene et al., 2000) .

Chapter 3: Microsecond Simulations of Amyloid Beta Fibril Nucleation in Reverse Micelles

This work made use of the Extreme Science and Engineering Discovery Environment (XSEDE), supported by National Science Foundation grant number OCI-1053575, and the Bridges system , at the Pittsburgh Supercomputing Center (PSC) supported by NSF award number ACI-1445606. Access to the Anton machine was made possible by the National Center for Multiscale Modeling of Biological Systems through grant number MCB150023P from the Pittsburgh Supercomputing Center.

I thank Görkem Eskici for assistance with figure design.

3.1 - Overview

Previously published experimental studies have suggested that the 40-residue amyloid beta peptide folds into a structure that may nucleate amyloid fibril formation when it is encapsulated in a reverse micelle (Yeung and Axelsen, J. Am. Chem. Soc. 134:6061, 2012). The factors that induce the formation of this structure have now been identified in a multi-microsecond simulation of the same reverse micelle system that was studied experimentally. Key features of the peptide-micelle interaction include the anchoring of a hydrophobic residue cluster into the reverse micelle surface, the formation of a beta turn at the anchor point that brings N- and C-terminal segments of the peptide into proximity, high ionic strength that dehydrates the peptide and promotes intramolecular hydrogen bond formation, and deformation of the reverse micelle surface so as to envelop the folded peptide and facilitate interactions with the surface along the entire length of the peptide. Together, these features cause the simulation-derived vibrational spectrum to red shift in a manner that reproduces the red-shift previously reported experimentally. On the basis of these findings, a new mechanism is proposed whereby membranes nucleate fibril formation and facilitate the in-register alignment of polypeptide strands with extended beta structure that is characteristic of amyloid fibrils.

3.2 -Introduction

Amyloid beta (Aβ) peptides are the unstructured cleavage products of a common membrane protein in the brain. In Alzheimer’s disease, they undergo a conformational change and aggregate into fibrils with in-register parallel β-sheet structure. The fibrils then coalesce into amyloid plaques, which are centers of oxidative stress and neuronal death, so the conditions that induce fibril formation are of high interest.

Fibril formation proceeds through a nucleation-dependent mechanism (Fezoui & Teplow, 2002; Lomakin, Chung, Benedek, Kirschner, & Teplow, 1996) and may be initiated by misfolded “seeds” (Terzi et al., 1997; Kirkitadze et al., 2001). While the critical concentration for *in vitro* fibrillation nucleation is micromolar (Lomakin et al., 1996; Sabate & Estelrich, 2005; Soreghan, Kosmoski, & Glabe, 1994), the concentration of Aβ peptides in the cerebral spinal fluid is subnanomolar (Seubert et al., 1992).Therefore, the relevance of fibril nucleation observed at high peptide concentrations to *in vivo* fibril formation is not clear. *In vivo,* the nucleation of fibril formation may involve an interaction between Aβ peptides and lipid membranes. However, it is difficult to study Aβ-membrane interactions relevant to the nucleation of fibril formation when fibril formation actually occurs.

To isolate the interaction between Aβ monomer and lipid membrane for experimental study, Aβ40 (the 40-residue Aβ peptide) has been encapsulated in reverse micelles (RMs). To preclude aggregation, no more than one peptide was present in each micelle, and only ~1% of the micelles contained a peptide. Surprisingly, the infrared amide I spectrum of the encapsulated peptide resembled that of a mature amyloid fibril, suggesting that one or more aspects of the RM environment may be responsible for nucleating fibril formation.

To characterize this structure, and identify the elements of an RM that induce its formation, a series of molecular dynamics simulations have been performed on a model system that corresponds precisely to the RM system examined experimentally. The model system was simulated for 3 microseconds using an Anton supercomputer. This simulation reveals an array of interactions that anchor the peptide into the surfactant layer and induce the formation of secondary structure. The behavior of the peptide within the RM suggests a new mechanism whereby polypeptide strands may be aligned in-register – an essential early step in the nucleation of amyloid fibrils.

3.3 -Methods

3.3.1 -Software, Hardware, and Parameters

All minimizations and all equilibration simulations were performed with NAMD2.9 (Phillips et al., 2005) and the CHARMM27 all atom force field for proteins and lipids (Foloppe & MacKerell, Jr., 2000). Parameters for the AOT anion and isoO were obtained from previously published studies (Abel et al., 2004; Abel et al., 2010; Tian & Garcia, 2011b; Martinez, Malolepsza, Rivera, Lu, & Straub, 2014b). Production runs were either performed on a local 32-node Linux cluster using NAMD2.9 or on 512-node Anton supercomputer for molecular dynamics (Shaw, Dror, Salmon, & Grossman, 2009). Systems were equilibrated as NPT ensembles, long-range electrostatic forces were calculated with the Particle Mesh Ewald method (Darden et al., 1993), an interaction cutoff of 12 Å was applied within periodic boundary conditions, and Van der Waals (VdW) forces were smoothly shifted to zero between 10 Å and 12 Å. Equations of motion were integrated with the Verlet method and a time step of 2 fs. Langevin dynamics with a damping coefficient of 5 ps^{-1} was used to keep the temperature at 293 ºK. The pressure was maintained at 1 atm using a Nosé-Hoover-Langevin piston (Feller et al., 1995). Coordinates were saved every 0.002 ns.

The systems simulated on Anton were propagated for 20 ns using NAMD 2.9 on the local 32-node Linux cluster before transferring systems to the Anton machine for long timescale simulations. Simulation procedure and times were summarized in Figure 3.1. Anton simulations were performed at 293 K using the Nosé-Hoover thermostat and the MTK barostat. The cutoff for VdW and short-range electrostatic interactions was 9.79 Å. Long-range electrostatic interactions were computed using the Gaussian split Ewald method (Shan et al., 2005) with the 64 × 64 × 64 grid size. Coordinates were saved every 0.24 ps.

3.3.2 -System Design, Equilibration, and Simulation

Aβ40 was created as extended linear chain with Pymol 1.8 (2016) and minimized for 2 ps in vacuo with NAMD. Starting structures for polypeptide with other sequences were created by mutating the side chains with Visual Molecular Dynamics (VMD) (Humphrey et al., 1996). An alternative starting structure was prepared by creating a polypeptide with the scrambled sequence as an extended linear chain with Pymol 1.8 (2016), minimizing for 2 ps in vacuo with NAMD and mutating side chains back to the wild-type sequence with VMD.

Simulation systems in which peptides were encapsulated in RMs were constructed with $W_0 = 11.4$, the value used in our earlier experimental study (Yeung & Axelsen, 2012) and $n_{AOT} = 127$, the result of equation 7-e in our earlier theoretical study (Eskici & Axelsen, 2016). The number of water molecules was $n_{water} = W_0 \times n_{AOT} = 1448$.

Peptides were solvated in a spherical cluster of $(n_{water} + n_{AOT} + 3)$ water molecules. AOT molecules were added by replacing n_{AOT} randomly selected water molecules with sodium cations, and distributing the anionic portions randomly on the surface of the cluster with SO_3 groups oriented inward. An additional 3 randomly selected water molecules were replaced with sodium cations to neutralize the –3 charge of the peptides. Next, these peptide/water/AOT systems were placed in the center of a cube with a length of 105 Å that contained 2899 molecules of isoO (n_{ISO}) – a number chosen so that the isoO mass was 84% of the total system (i.e. system containing peptide, water, AOT and isoO) mass and thus, within the RM-forming portion of the AOT/water/isoO phase diagram (Abel et al., 2010). A separate RM simulation system was constructed with the same method and composition, but with 202 fewer water molecules, corresponding to the volume of an Aβ40 peptide (~6050 $Å^3$).

Four water box systems were also created with the VMD solvation plugin, using the coordinates of the peptide and a cubic shape with an edge length of 66 Å. As in the RM systems, the VMD ionization plugin was used to replace 3 randomly selected water molecules with sodium cations to neutralize the system. In one of the four systems, the peptide was unconstrained, while in a second system, 5 kcal/mol constraints were applied to peptide to constrain it to a 20 Å sphere to mimic RM encapsulation. In a third system, the peptide was unconstrained, and 3 M NaCl was used to mimic 6 M sodium cation concentration in RM. The fourth system included both the spherical constraint and 3M NaCl.

RM systems were energy minimized in six stages, each stage consisting of 0.01 ns minimization and 1 ns of NPT simulation. In stage one, all atoms except those in the isoO solvent were fixed in position. In stage two, the hydrocarbon tails of the AOT anions were unfixed. In stage three, the remaining portions of the AOT anions were unfixed. In stage four, water and sodium cations were unfixed. In stage five, side chains of protein were unfixed. In stage six, all molecules in the system were unfixed. WB systems were energy minimized with only the latter three stages.

3.3.3 -Analysis

Eccentricities were calculated as described previously (Eskici & Axelsen, 2016). Various VMD plugins were used for analysis. The TIMELINE and STRIDE plugins were used to characterize secondary structure by phi/psi angle and hydrogen bond criteria. The NAMD ENERGY plugin was used to calculate VdW interaction energies. The SASA plugin with a 1.4 Å solvent probe was used to calculate solvent accessible surface area.

The IR Spectral Density Calculator plugin was used with default settings and a temperature of 293 K to calculate vibrational spectra in the amide I region of the infrared spectrum. This plugin requires a protein structure file and trajectory as input data, and calculates a vibrational spectral density through a Fourier transform of dipole autocorrelation functions. To obtain frequencies with a resolution of 2 cm^{-1}, a trajectory saved at 1 fs intervals was required. Because simulations performed on Anton cannot be saved at less than 240 ps intervals, snapshots were sampled at 50 ns intervals from equilibrated Anton simulations, the polypeptide coordinates was excerpted from these snapshots, and the motions of the main chain atoms were simulated *in vacuo* for 16 ps using NAMD with side chain atom positions fixed to prevent structural distortion. To correct for the ~50 cm^{-1} blue shift that invariably occurs when predicting infrared spectra from molecular mechanics simulations, frequencies resulting from this procedure were scaled by 0.97. The intrinsic line width of each frequency was modeled as a Lorentzian distribution with a full-width at half-maximum of 8 cm^{-1}, and the distributions were summed to yield a spectrum. Finally, the amplitudes of the spectra for each snapshot were averaged and the maximum amplitudes were normalized.

3.4 -RESULTS:

3.4.1 -Initial Structures and Conditioning

The procedures described above yielded 10 simulation systems: 6 RM and 4 water box systems (Table 3-1). These included one RM system containing the wild type Aβ40 sequence (WT), and a second system that was identical except for an alternative backbone conformation (WT_{Alt}). A third RM system had a scrambled amino acid sequence (SC), while a fourth system had only15-21 scrambled (WT_{SC}). A fifth system was identical to SC, except that the wild-type sequence of amino acids 15-21 was restored (SC_{WT}). Peptide sequences are given in Table 3-2. The sixth system was identical to WT except that a volume of water equivalent to the volume of the peptide was removed (WT_{202}). Each of the six RM systems began with a single polypeptide strand, bearing no recognizable secondary structure or intramolecular hydrogen bonding, positioned at the center of a spherical RM with a radius of 20 Å and all residues at least 5 Å from the surfactant.

The 4 water box systems included one with an Aβ40 peptide placed in the center of a water box (WB). A second system was identical to WB except that the polypeptide was restrained to a soft but non-deformable 20 Å sphere (WB_C). A third water box system had no restraints but included 3M sodium chloride to mimic the high internal ionic strength of the WT system (WB_I). The fourth water box system included both the spherical constraint and 3M sodium chloride (WB_{CI}).

After energy minimization, RM systems were conditioned by simulating them as NPT ensembles for 20 ns using NAMD 2.9, to eliminate instabilities that cause them to crash with "momentum exceeded" errors on Anton. During the 20 ns conditioning period, the shape of each RM became markedly non-spherical, although all portions of the polypeptide remained at least 3 Å from the surfactant. The four water box systems were not run on Anton, so they did not require conditioning, but they were conditioned for 20 ns anyway to facilitate comparison with the RM systems. During conditioning, the edge length of the water box systems shortened to 62.5 Å. In WB_C and WB_{CI}, all peptide residues remained at least 0.5 Å from the restraint limit.

3.4.2 -Equilibration

The overall system energies and volumes in all 10 simulation systems reached apparent equilibrium values during the 20 ns conditioning periods. During subsequent simulations, there was no net water gain or loss from the RMs, and water molecules were only rarely observed in the isoO phase. Therefore, the energies, volumes, and water contents of each RM system appeared to be well equilibrated at the end of the 20 ns conditioning periods. However, the WT and SC systems required approximately 200 ns for eccentricity values to plateau, while the eccentricity values of the other systems appeared to require less than 100 ns (Figure 3.2). The evolution of polypeptide conformation within each system was evaluated (Figure 3.S1), and most every secondary structure that eventually formed in any system had formed within 200 ns.

Therefore, we concluded that all systems were suitably equilibrated by 200 ns, and subsequent analyses were only performed on portions of the simulations beyond 200 ns.

3.4.3 -Polypeptide interactions with RM surface

In each RM system, gaps large enough to pass a water molecule were frequently observed in the RM surface between surfactant molecules (Figure 3.3). Some of these gaps were filled by isoO, permitting direct contact between isoO molecules and components of the RM core. Other gaps were filled by hydrophobic amino acid side chains, which consequently made direct contact with both the isoO and the hydrocarbon tails of the surfactant.

There are three possible explanations for the occurrence of these surface gaps. One is that they form because deviations from a spherical shape increase the surface-area-to-volume ratio to a point where AOT molecules cannot cover the surface. A second possible explanation is that peptide encapsulation causes the RM volume to expand to a point where AOT molecules cannot cover the surface. A third possible explanation is that side chain insertion into the surface is energetically favorable and thereby creates gaps that would not otherwise exist. These possibilities are not mutually exclusive.

To evaluate these possibilities, SASAs were determined for each structure snapshot saved from the last 100 ns of each of the 6 simulation systems, as well as from an RM simulation identical to the WT system except without encapsulated peptide (designated RM_{127} because all of these RM systems have 127 AOT molecules). The total SASA, and individual contributions of water, sodium ions, protein, and AOT to the SASA, were averaged separately (Figure 3.4). The “gap area” was defined as the sum of the SASAs for water, sodium ions, and protein, and is represented as a percentage of total SASA.

Results show that the peptide-free RM_{127} system and the peptide-containing WT_{202} systems had the smallest gap areas. Because the only difference between these two systems was the presence of peptide, and waters were removed to compensate for peptide volume in the WT_{202} system, it appears that gaps form due to shape distortion of the RM, irrespective of whether an encapsulated peptide was present. In other simulation systems, where water molecules were not removed to compensate for the added volume of the encapsulated peptide, gap areas were invariably larger. These results show that the expansion of RM volume by peptide encapsulation also increased gap area.

Although the WT_{202} and RM_{127} systems had similar gap areas as a percentage of total SASA, the total SASA for RM_{127} was much larger than the total SASA for WT_{202}. The most significant contributions to the larger SASA of RM_{127} were due to the SASAs of AOT molecules and waters. Since the number of AOT molecules was the same in both systems, the larger AOT area is likely due to a larger portion of AOT molecules being solvent exposed, either through a change in their shape, or because the “side” of an

AOT molecule became accessible to the 1.4 Å surface area probe. In the other 5 polypeptide-containing RM systems (WT, WT_{Alt}, WT_{SC}, SC, and SC_{WT}) gap areas varied with the total SASA, as would be expected in systems with the same fixed number of AOT molecules.

To quantify the number and size of the gap areas, and the extent to which amino acid side chains occupied those, VdW interaction energies were calculated between each amino acid side chain and the set of all isooctane molecules (Figure 3.5). Hydrophobic side chains in the WT, WT_{Alt}, and WT_{202} systems tended to have larger interaction energies than in other systems. Visual inspection of these simulations confirmed that the side chains of Leu17, Phe19 and Phe20 typically situated in the gaps between surfactant molecules, making contact with AOT tails and isoO molecules. Overall interaction energies were markedly smaller in the SC and WT_{SC} systems, but the relatively large interaction energies between Phe19, Phe20 and isoO were restored in the SC_{WT} system. These observations suggest that the chemical context of the polypeptide side chains (i.e. the sequence) influenced the extent to which hydrophobic side chains occupied gaps in the surfactant layer. More specifically, this observation suggested that the clustering of hydrophobic side chains promoted their association with gaps.

We conclude that gap formation occurs regardless of peptide presence, but that an encapsulated peptide increased gap formation. The occupation of surface gaps by hydrophobic side chains appears to be energetically favorable, particularly when they are clustered together in sequence. However, the energetics and/or extent of this interaction were insufficient to cause a detectable increase in gap area.

3.4.4 -Polypeptide orientation and conformation

Visual inspection of the simulation trajectories revealed significant differences in the way that polypeptides situated within the RMs. The polypeptides in the WT, WT_{Alt}, WT_{202}, and SC_{WT} systems tended to associate with the surfactant and distort the RM shape to closely envelope them. The SC and WT_{SC} systems, in contrast, assumed central positions within the RM. These differences are evident in Figure 3.6, where the larger numbers of sulfate groups within 3 Å of the polypeptides in the WT, WT_{Alt}, WT_{202}, and SC_{WT} reflect their overall closer proximity to the surfactant headgroups.

Differences in secondary structure propensities for each residue were determined by calculating the fraction of time that they are in a random coil, turn, helix, β–strand and turn (Figure 3.7). The most prominent feature of the WT system was a β turn involving residues 18-21 that persisted throughout the 3 μs simulation (Figure 3.8). This turn was also evident in the WT_{Alt}, WT_{202}, and SC_{WT} systems, but not in the SC and WT_{SC} systems, indicating that the clustering of these residues in sequence was required for β turn formation. In view of this observation, it should be recalled that the side chains of the residues involved in this turn are the same side chains that tended to insert into gaps between surfactant molecules on the RM surface (Figures 3.3 and 3.5).

Thus, Aβ40 within a reverse micelle appears to assume a hairpin shape with a stable β turn, hydrophobic side chains projecting from the end of the hairpin into the surfactant, and the remainder of the polypeptide enveloped by surfactant (Figure 3.9).

The secondary structures of polypeptides in WB systems were also characterized (Figure 3.10). There was no persistent secondary structure in the WB system, although a persistent α-helix formed in WB_C involving residues 11-16, and several short stretches of extended β-sheet formed in WB_I. The WB_{CI} system formed various turns involving residues 17-25, but not the β turn observed in the WT system involving residues 18-21. Therefore, we conclude that while confinement and high ionic strength appear to promote the formation of turns, interactions with surfactant are required to form the stable β turn at residues 18-21.

3.4.5 -Predicted vibrational spectra

Vibrational spectra were calculated for the amide I vibration of the polypeptide in the WT, WT_{Alt}, WT_{202} and SC systems and compared to that of the initial random coil (Figure 3.11). The SC and random coil spectra were broad and centered at 1640 cm^{-1}. However, spectra for the WT, WT_{Alt}, and WT_{202} systems were shifted to 1630 cm^{-1}. The higher frequency amide I components (1670-1690 cm^{-1}), usually assigned to the β turns that are prevalent in all of these simulations, do not appear in the calculated spectra because N-H bond lengths in these simulations are fixed. Aside from these high frequency bands, therefore, the calculated spectra for WT, WT_{Alt}, WT_{202} are consistent with the previously published experimental IR spectra obtained from Aβ40 encapsulated in an RM.

3.5 -Discussion

This investigation provides detailed insight into previously published experimental observations about the remarkable behavior of Aβ40 peptides encapsulated in RMs. Those experimental observations suggested that how the RM environment may induce monomeric Aβ40 to nucleate amyloid fibril formation. The most striking result of this study is that the simulations reproduce the experimentally observed red-shift in the amide I vibrational spectrum that is characteristic of amyloid fibril formation. Experimentally, this shift is due to the alignment and coupling of amide I oscillators – chiefly the N–C=O groups in the polypeptide backbone. In molecular mechanics simulations, these effects are modeled by electrostatic interactions between fixed partial charges. More sophisticated analyses based on transition dipole coupling may be performed, but with only modest improvements in accuracy, and these analyses still depend on molecular mechanical simulations to create a suitable ensemble of structures.

The insight provided by the current investigation shows that Aβ40 has 3 distinct types of interactions with components of the RM. One interaction is between the surfactant layer and a hydrophobic cluster composed of residues 17-21. In particular, the side chains of Phe19 and Phe20 insert into gaps between AOT molecules, thereby anchoring the peptide in the RM surface through hydrophobic interactions. Steric interactions between the Phe side chains then promote β turn formation, while electrostatic interactions between their π-electron systems stabilize an edge-to-face interaction (Burley & Petsko, 1986; Burley & Petsko, 1985) (Figure 3.8). This arrangement of aromatic rings and β turn formation is in excellent agreement with previously published NMR results (Zhang et al., 2000), and with numerous experimental studies showing the importance of Phe19 and Phe20 for folding (Sikorski, Atkins, & Serpell, 2003), fibril formation (Esler et al., 1996; Wurth, Guimard, & Hecht, 2002; Makin, Atkins, Sikorski, Johansson, & Serpell, 2005; Cukalevski et al., 2012; Bernstein et al., 2005), dimer formation

(Gnanakaran, Nussinov, & Garcia, 2006,) and lipid membrane interactions (Di Scala et al., 2013).

A second interaction is between the polypeptide and ions in the RM interior. By competing for available water in the hydration shells, ions tend to dehydrate the polypeptide and promote the formation of intramolecular hydrogen bonds. This conclusion is supported by spectroscopic studies showing that high ionic concentration induces a transition from random coil to β-sheet in Aβ (Jarvet, Damberg, Bodell, Eriksson, & Graslund, 2000) .

A third interaction is between the surfactant layer and the whole polypeptide. The RM surface is highly deformable and porous. This deformability facilitates more extensive interactions between polypeptide and the surfactant layer than would otherwise be possible if the surface was rigid (Figure 3.9), and it explains why two salient aspects of the RM environment – physical confinement and crowding – do not appear to affect Aβ behavior. With the polypeptide anchored in the membrane and enveloped by it, there is a large portion of the RM interior that is not occupied by the peptide. Any reduction in the configurational entropy of the polypeptide is due to localized polypeptide-membrane interactions, rather than confinement or crowding. This conclusion is supported by the experimental finding that Aβ behavior is similar in an RM with W_0=11.4 or W_0=30 (Yeung & Axelsen, 2012).

Overall, the forgoing results are in excellent agreement with a recent but much more limited NMR and simulation study of the Aβ(16-28) segment, which also found that the hydrophobic cluster spanning residues 17-21 mediates the association of this segment with membranes (Bera et al., 2016). Most previously published simulation studies of Aβ-membrane interactions, however, have been performed with simpler peptide models that cannot mimic the features critical to the findings of this study, such as hydrogen bonds and aromatic ring interactions (Davis & Berkowitz, 2009b; Davis & Berkowitz, 2009a), while others have been performed with simplified (Mobley, Cox, Singh, Maddox, & Longo, 2004; Xu et al., 2005; Lemkul & Bevan, 2011; Lemkul & Bevan, 2009; Davis & Berkowitz, 2009a; Brown & Bevan, 2016) or heterogeneous (Manna & Mukhopadhyay, 2013; Zhou & Xu, 2012; Lemkul & Bevan, 2013; Zhao, Chiu, Benoit, Chew, & Mu, 2011) membrane models. Still other simulation studies begin with pre-inserted peptide (Lemkul & Bevan, 2008; Xu et al., 2005; Lemkul & Bevan, 2009; Lemkul & Bevan, 2011) or multiple peptides (Brown & Bevan, 2016) to study mechanisms of oligomerization and aggregation. Many of these studies also address questions about fibril nucleation, but the strength of the current results is that they focus on the Aβ monomer under simulation conditions that precisely mimic the conditions that have been characterized experimentally.

These results are significant to questions about how Aβ peptides are induced to form amyloid fibrils in Alzheimer's Disease. Aβ peptides are normally present in human brain, but they are neither aggregated nor structured. Their conversion into an amyloid fibril with highly regular structure is a nucleated process that is likely to involve interactions with a membrane (McLaurin & Chakrabartty, 1997; Terzi, Holzemann, & Seelig, 1995; Sabate, Gallardo, & Estelrich, 2005; Kremer, Pallitto, Sklansky, & Murphy, 2000; Kremer, Sklansky, & Murphy, 2001). These interactions are difficult to study experimentally because they are obscured by the aggregation that ensues, but RM encapsulation prevents aggregation and makes interaction of the peptide with a membrane experimentally accessible.

In conjunction with the previously published experimental results, several pathways and intermediates were proposed by which monomeric peptides may aggregate to form fibrils. Two key steps in these pathways are (1) the alignment of polypeptide chains so that the β sheets are in-register , and (2) the rotation of peptide main chains to create intermolecular rather than intramolecular hydrogen bonds. It was supposed that this alignment might be due to the coordination of a copper ion to the His residues at positions 13 and 14 in two different Aβ peptides. The current study shows that alignment may also be a consequence of Phe19-Phe20 residues from two different Aβ peptides both anchoring in the same membrane. Overall, these results are consistent with previously reported experimental results, and provide invaluable insight into the molecular details underlying those results, with clear implications for the nucleation of amyloid fibrils and the pathogenesis of Alzheimer's disease.

Table 3.1 - Compositions of simulated systems*

System Name	Conformation	n_{water}	n_{sod}	n_{cl}	n_{AOT}	n_{ISO}	n_{atoms}	f_{iso} (%)	r_W (Å)	s (Å)
WT	1	1448	130	-	127	3926	115403	87	20	105
WT_{Alt}	2	1448	130	-	127	3846	113323	87	20	105
SC	1	1448	130	-	127	2899	88701	84	20	96
WT_{SC}	1	1448	130	-	127	2899	88701	84	20	96
SC_{WT}	1	1448	130	-	127	2899	88701	84	20	96
WT_{202}	1	1246	130	-	127	2899	88095	84	20	96
WB	1	8275	3	-	-	-	25426	-	-	66
WB_C	1	8275	3	-	-	-	25426	-	-	66
WB_I	1	7302	487	487	-	-	23478	-	-	66
WB_{CI}	1	7302	487	487	-	-	23478	-	-	66

*n_{water}, n_{sod}, n_{cl}, n_{AOT}, n_{ISO}, and n_{atoms} are the numbers of water molecules, sodium cations, chloride anions, AOT, isooctane molecules. n_{atoms} is the total number of atoms in each system. f_{iso} is the mass fraction of isoO as a percentage of mass of all components in the system. r_W is the average distance from the center of the RM to the outermost water molecule. s is edge length of the unit cell. All RM systems had been started from the same number of isooctane. Extra isooctane molecules were added to WT and WT_{Alt} to increase the distance between RMs in adjacent periodic images, as RM structures in these systems elongated dramatically.

Table 3.2 - Sequences used in this study

Name	**Sequence**
WT	DAEFR HDSGY EVHHQ KLVFF AEDVG SNKGA IIGLM VGGVV
SC	KVKGL IDGDH IGDLV YEFMA SNSFR EGVGA GHVHV AQVEF
$\mathrm{WT}_{\mathrm{SC}}$	DAEFR HDSGY EVHHF KAVQL FEDVG SNKGA IIGLM VGGVV
$\mathrm{SC}_{\mathrm{WT}}$	YVKGE IDGDH IGDLQ KLVFF ANSFR EGVGA GHVHV AMVES

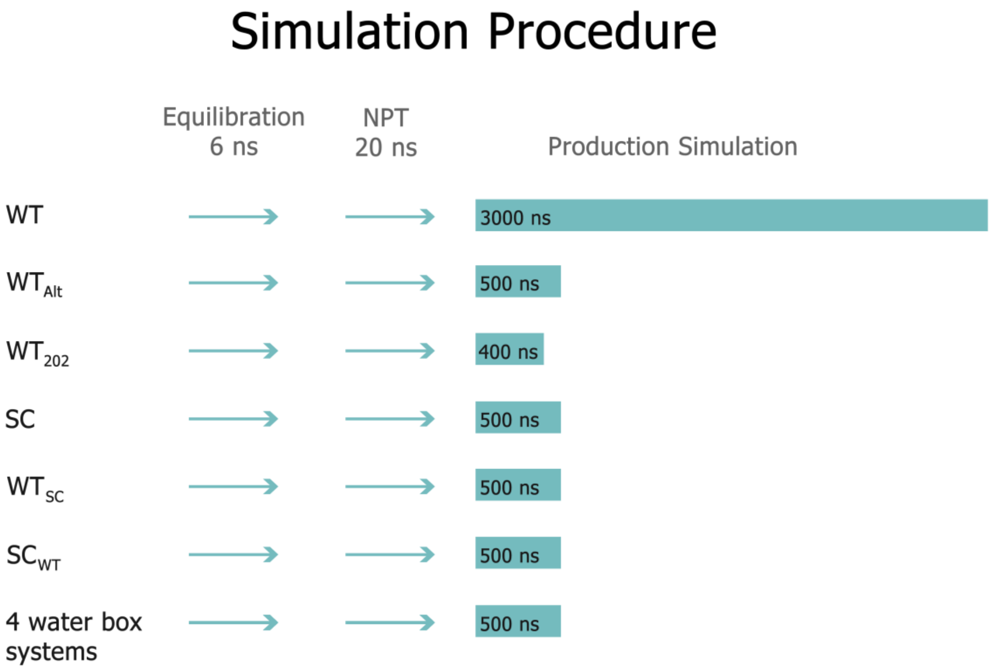

Figure 3.1 - Summary of simulation procedures followed for six RM systems and four water box systems.

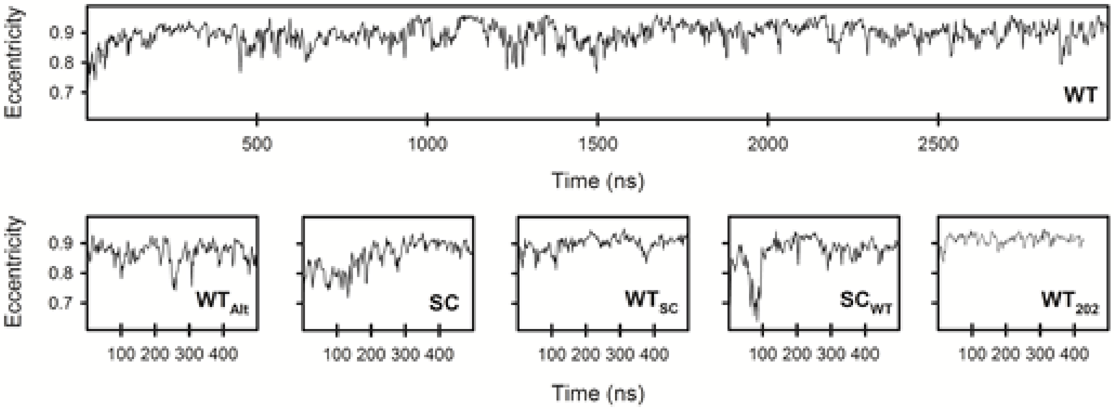

Figure 3.2 - Eccentricity of RM shape vs time.
Upper panel: eccentricity of the WT system throughout 3000 ns; Lower panel: eccentricity of WT_{Alt}, SC, WT_{SC}, SC_{WT} and WT_{202} systems throughout 500 ns.

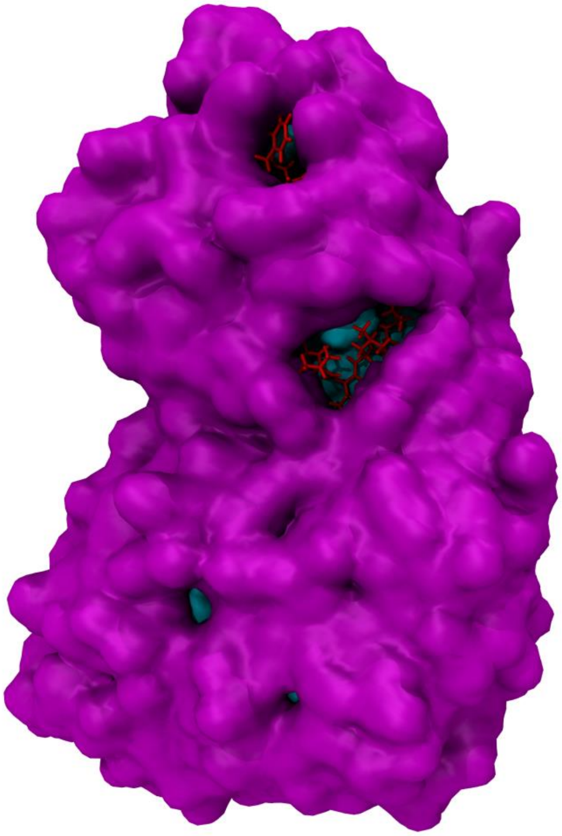

Figure 3.3 - A sample snapshot from simulation of the WT system showing gaps in the surface by surfactant coverage and occupation of these gaps by hydrophobic residues.
The structure is illustrated by representing protein with red licorice model, water molecules as cyan surface, and AOT anions as purple surface.

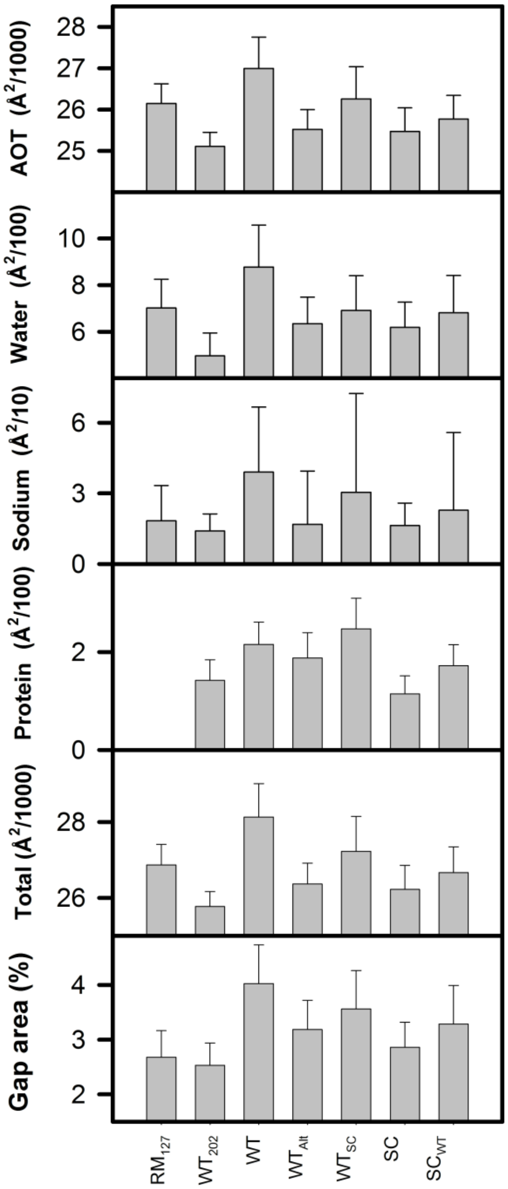

Figure 3.4 - isoO accessible surface areas of system components and gap area in the surfactant layer (i.e. the sum of the SASAs for water, sodium ions, and protein) as a percentage of total SASA

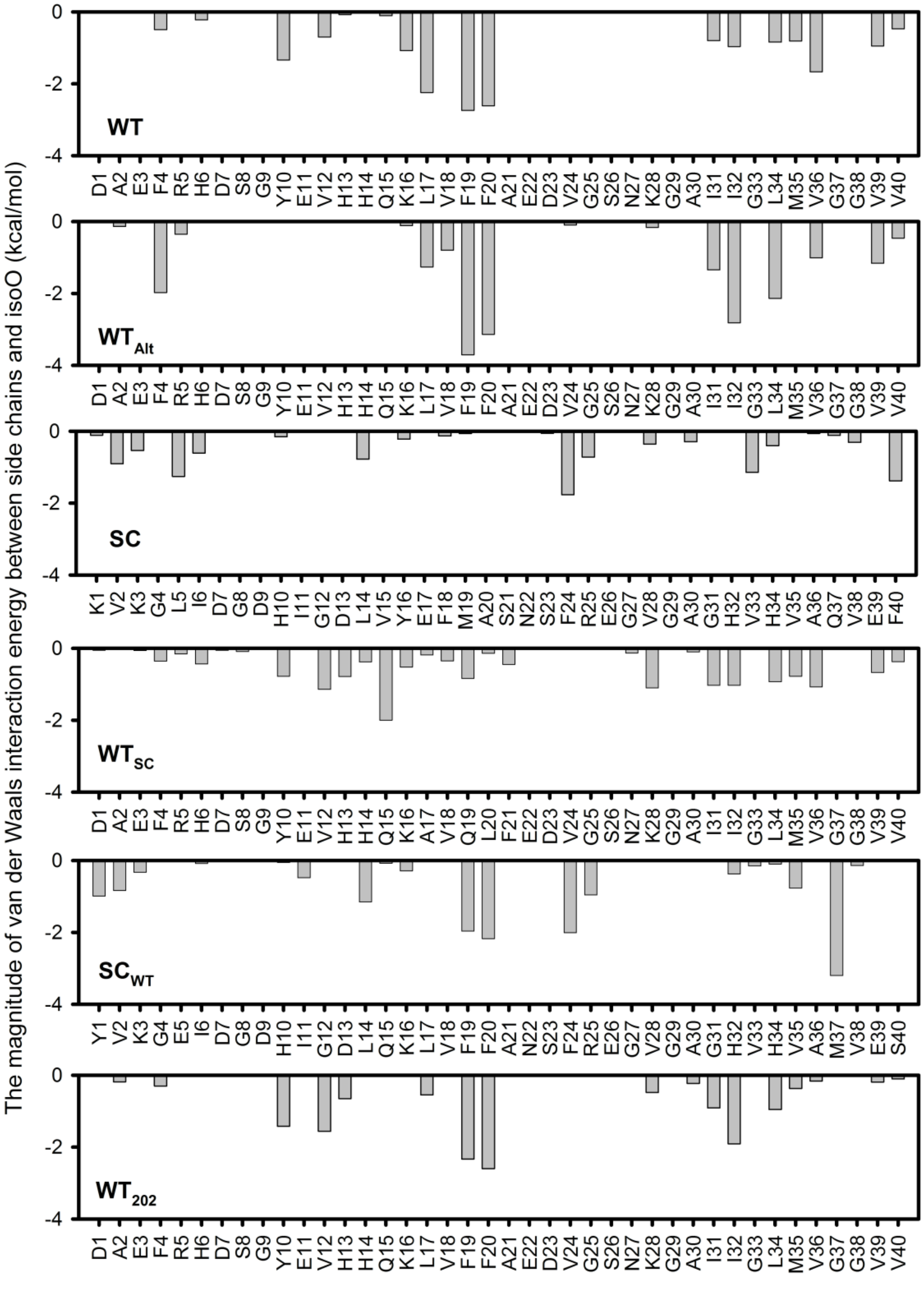

Figure 3.5 - Magnitudes of van der Waals interaction energies between side chains and isoO.

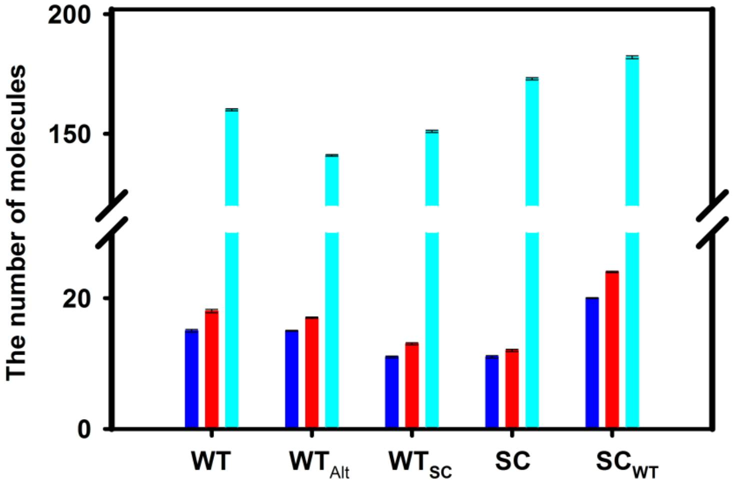

Figure 3.6 - Average number of sodium ions, SO3 groups and water molecules within 3 Å of polypeptides in RM systems.
Standard errors were shown with double-sided bars.

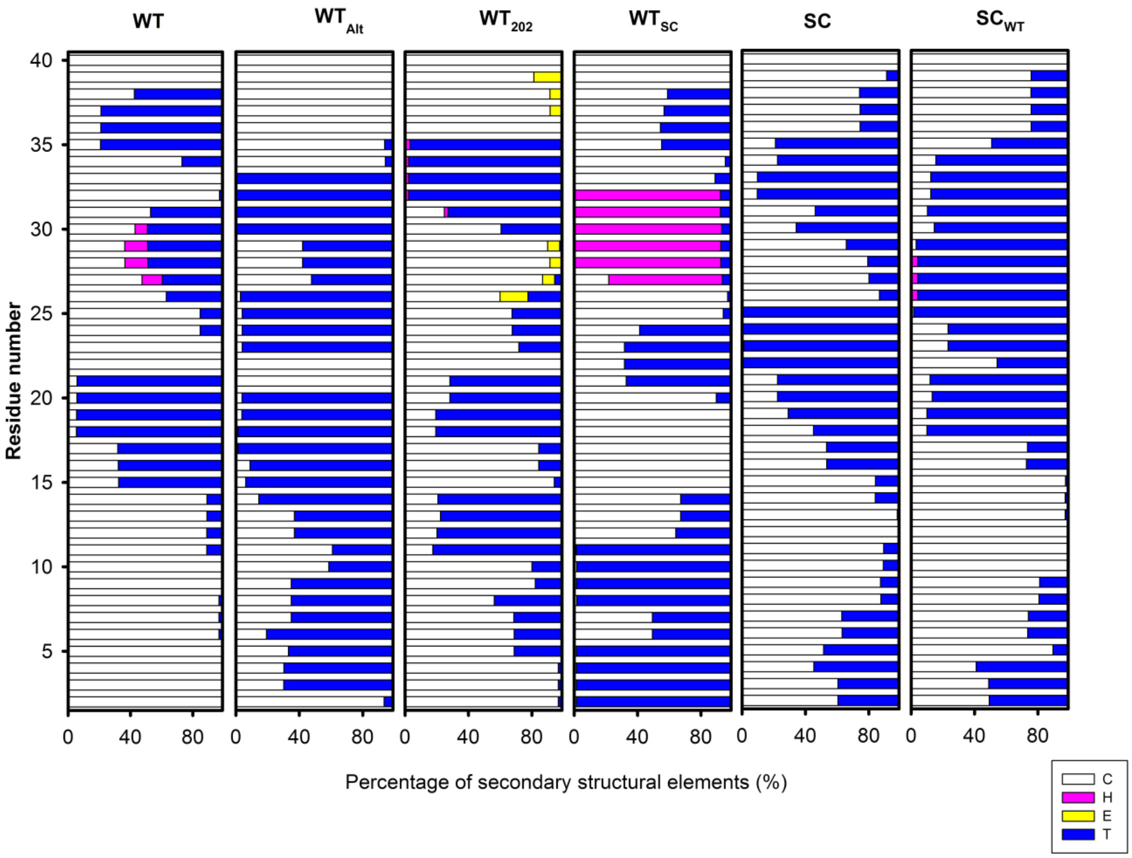

Figure 3.7 - Random coil, helix, β–strand and turn forming propensities of residues in RM systems.

This figure is derived from Figure 3-S1 by calculating the fraction of time that each residue is in a random coil, turn, helix, β–strand and turn.

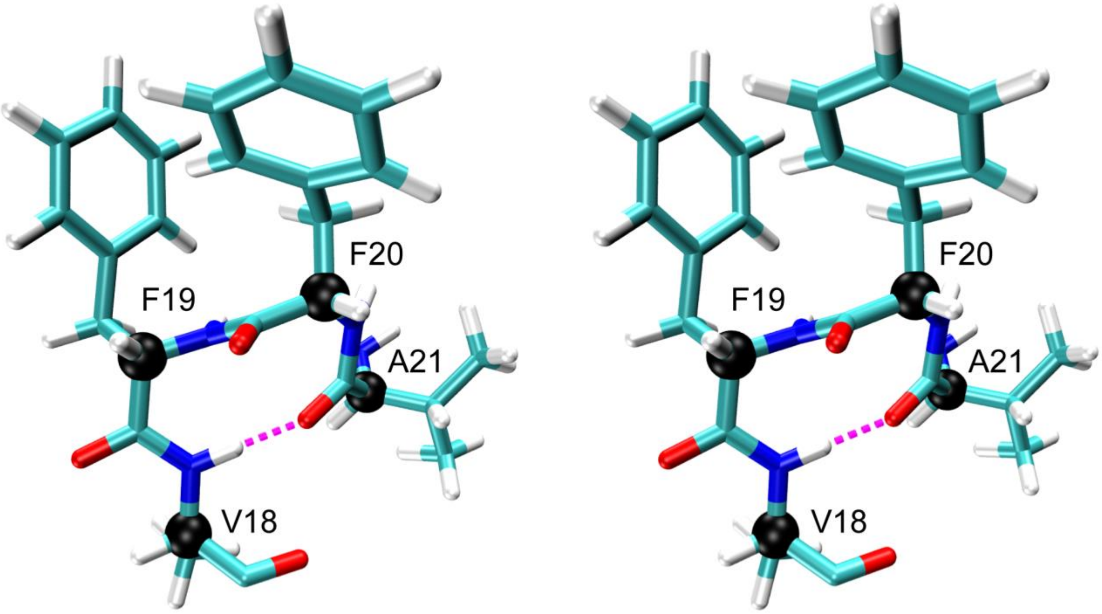

Figure 3.8 - Wall-eyed stereo images of the turn involving residues 18-21 showing edge-to-face orientation of phenylalanine side chains and hydrogen bonding between Val18 and Ala21.

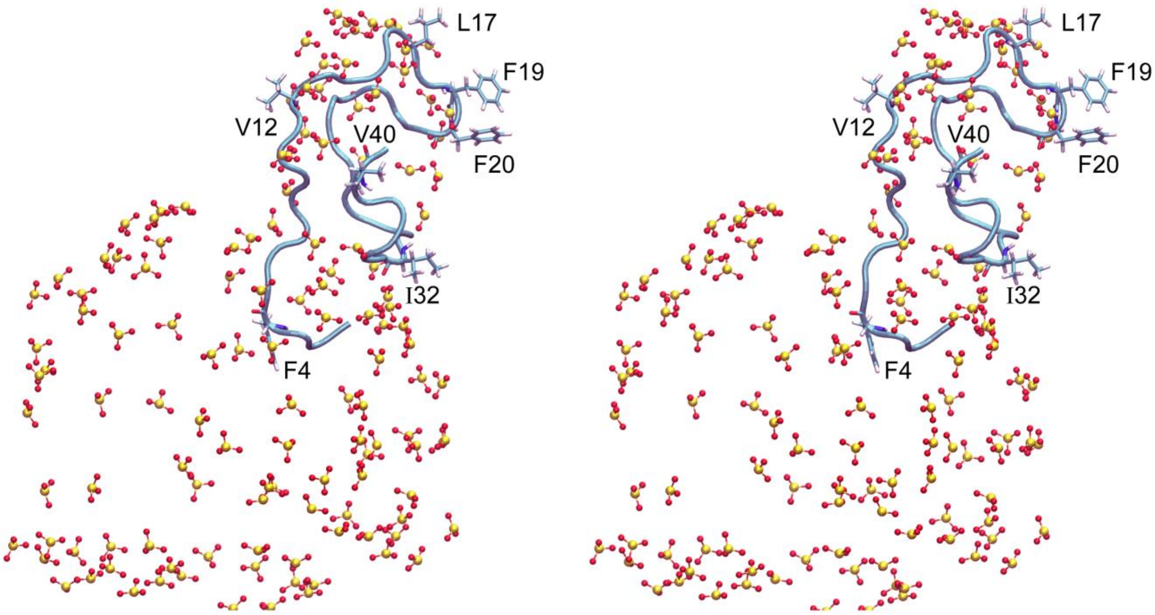

Figure 3.9 - Wall-eyed stereo images of encapsulated polypeptide and SO_3 headgroups of AOT from the simulation of WT system.
This figure is illustrated by representing protein main chain as cyan ribbon, hydrophobic side chains as licorice, and SO_3 headgroups of AOT with CPK model.

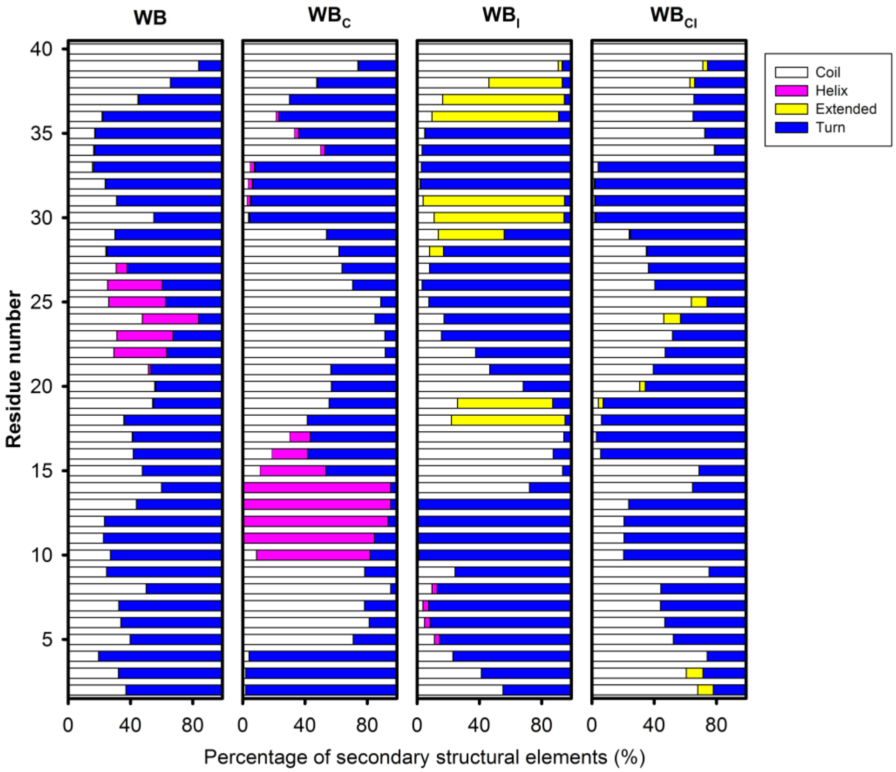

Figure 3.10 - Random coil, helix, β–strand and turn forming propensities of residues in WB systems.
This figure is derived from Figure S1 by calculating the fraction of time that each residue is in a random coil, turn, helix, β–strand and turn.

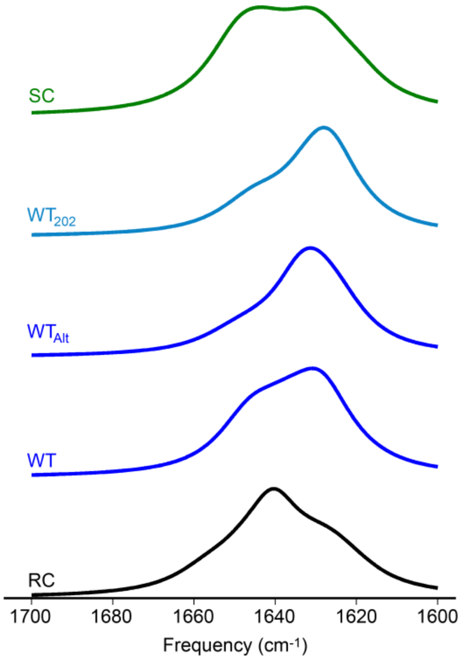

Figure 3.11 - Predicted vibrational spectra of initial random coil structure, the WT, the WT_{Alt}, the WT_{202}, and the SC.

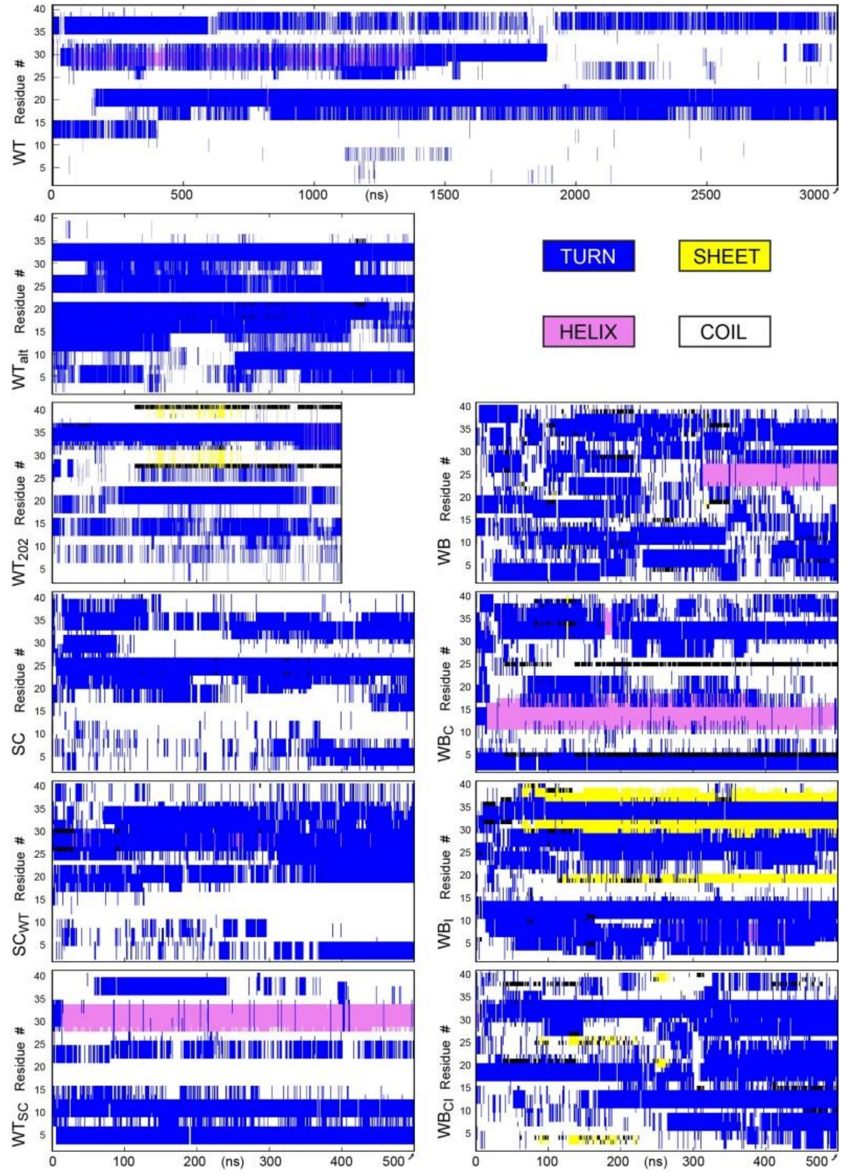

Figure 3.12 - Secondary structure evolution of polypeptides.

This figure is modified from TIMELINE plugin of VMD. (A) WT; (B) Top to bottom: WT_{Alt}, WT_{202}, SC, SC_{WT} and WT_{SC}; (C) Top to bottom: WB, WB_{C}, WB_{I}, WB_{CI} (Turns are represented in blue; random coils are represented in white; helices are shown in pink; extended-β sheets are represented in yellow.

Chapter 4: Intermicellar Exchange and Protein Encapsulation

This work made use of the Extreme Science and Engineering Discovery Environment (XSEDE), supported by National Science Foundation grant number OCI-1053575, and the Bridges system , at the Pittsburgh Supercomputing Center (PSC) supported by NSF award number ACI-1445606. Access to the Anton machine was made possible by the National Center for Multiscale Modeling of Biological Systems through grant number MCB150023P from the Pittsburgh Supercomputing Center.

I thank Dr. Kim Sharp for valuable discussion and Görkem Eskici for assistance with figure design.

4.1 -Introduction

Computational models of RMs are large, and therefore it is difficult to simulation a system of relevant size for lengths of time over which interesting phenomena can be studied. Accordingly, it is even more difficult to study multiple RMs and their interactions.

The rapid intermicellar exchange of RM components is well documented experimentally. The mechanism of exchange is unclear, but most likely involves collisions between RMs. These collisions constantly sustain their mean size on equilibrium. This mean size has been studied experimentally and theoretically. In Chapter 2, extensive MD simulations are described, and the physicochemical basis for the mean size was examined. The methodology involved pre-assembled spherical RMs, and there was only one RM in each system. Therefore, intermicellar interactions that might drive and facilitate the exchange of RM components to achieve a thermodynamic equilibrium could not be examined.

Access to an Anton 2 machine allowed us to create simulations systems with more than one RM and observe them over a microsecond timescale. The chief question we aim to answer with this allocation is whether patterns of intermicellar exchange will confirm or contradict earlier conclusions about RM size. It is of particular interest to explore the effects of protein encapsulation on RM size. Therefore, the systems to be studied include non-equivalent RMs, for example RMs that differ in size, or in the presence of an encapsulated polypeptide.

4.2 - Methods

4.2.1 -Software, Hardware, and Parameters

All minimizations and all equilibration simulations were performed with NAMD2.9(Phillips et al., 2005) and the CHARMM27 all atom force field for proteins and lipids (Foloppe & MacKerell, Jr., 2000). Parameters for the AOT anion and isooctane (isoO) were obtained from previously published studies (Abel et al., 2010; Abel et al., 2004; Tian & Garcia, 2011b; Martinez et al., 2014b). Production runs were performed on Anton 2 supercomputer for molecular dynamics (Shaw et al., 2014). Systems were equilibrated as NPT ensembles, long-range electrostatic forces were calculated with the Particle Mesh Ewald method (Darden et al., 1993), an interaction cutoff of 12 Å was applied within periodic boundary conditions, and Van der Waals (VdW) forces were smoothly shifted to zero between 10 Å and 12 Å. Equations of motion were integrated with the Verlet method and a time step of 2 fs. Langevin dynamics with a damping coefficient of 5 ps−1 was used to keep the temperature at 293 ºK. The pressure was maintained at 1 atm using a Nosé-Hoover-Langevin piston (Feller et al., 1995). Coordinates were saved every 0.002 ns.

The systems simulated on Anton 2 were propagated for 30 ns using NAMD 2.9 on the Bridges system provided by the Extreme Science and Engineering Discovery Environment (XSEDE) before transferring systems to the Anton 2 machine for long timescale simulations. Simulation procedure and times were summarized in Figure 4.1. Anton simulations were performed at 293 K using the Nosé-Hoover thermostat and the MTK barostat. The cutoff for VdW and short-range electrostatic interactions was 9.79 Å.

Long-range electrostatic interactions were computed using the Gaussian split Ewald method (Shan et al., 2005). Coordinates were saved every 0.24 ps.

4.2.2 -System Design, Equilibration, and Simulation

Initial structure of Aβ40 was created as described in Chapter 2 (See "System Design, Equilibration, and Simulation"). RMs were constructed with $W_0 = 11.4$, the value used in our earlier experimental study (Yeung & Axelsen, 2012). Normal size RM (***N***) included 127 AOT molecules, the result of equation 7-e in our earlier theoretical study (Eskici & Axelsen, 2016). The number of water molecules was $n_{water} = W_0 \times n_{AOT} = 1448$. While small size RM (***S***) had 63 AOT and 724 water molecules, large size RM (***L***) had 190 AOT and 2166 water molecules.

To construct normal size RM including Aβ40 (***Np***), the peptide was solvated in a spherical cluster of 1578 water molecules. AOT molecules were added by replacing 127 randomly selected water molecules with sodium cations, and distributing the anionic portions randomly on the surface of the cluster with SO_3 groups oriented inward. An additional 3 randomly selected water molecules were replaced with sodium cations to neutralize the –3 charge of the peptides.

Next, these RM systems were placed in a unit cell with size of (130 Å x 165 Å x 130 Å) that contained a number of isooctane (isoO) molecules (n_{ISO}) – a number chosen so that the isoO mass was 84% of the total system (i.e. system containing peptide, water, AOT and isoO) mass and thus, within the RM-forming portion of the AOT/water/isoO phase diagram (Abel et al., 2010).

Four RM systems were energy minimized in six stages, each stage consisting of 0.01 ns minimization and 1 ns of NPT simulation. In stage one, all atoms except those in the isoO solvent were fixed in position. In stage two, the hydrocarbon tails of the AOT anions were unfixed. In stage three, the remaining portions of the AOT anions were unfixed. In stage four, water and sodium cations were unfixed. In stage five, side chains of protein were unfixed. In stage six, all molecules in the system were unfixed. WB systems were energy minimized with only the latter three stages.

4.2.3 - Analysis

Interaction energies for each saved coordinate set were calculated using VMD and the same parameters used to create the trajectory (VMD and NAMD therefore yield identical energies for the same structure). These energies were averaged over all members of each species, and over all saved coordinate sets, for each simulation.

4.3 -Results

The simulations described in this chapter are ongoing, and only a preliminary analysis described below.

4.3.1 -Initial Structures and Conditioning

The procedures described above yielded 4 simulation systems (Table 4.1). These included one system containing two RMs with the number of AOT (nAOT = 127) predicted by our previous investigation for a Wo of 11.4 (***NN***). A second system was created containing one of these “normal sized” RMs and a second RM with half the number of AOT and waters (***NS***). A third RM system was created with one normal sized

RM and one that had 1 ½ times the number of AOT (***NL***). A fourth system was identical to ***NN***, except that one RM included a single molecule of Aβ40 (***NNp***). The peptide was positioned at the center of the RM, which has a radius of 20 Å. All residues were at least 5 Å from the surfactant.

After energy minimization, RM systems were conditioned by simulating them as NPT ensembles for 30 ns using NAMD 2.9, to eliminate instabilities that cause them to crash with "momentum exceeded" errors on Anton. During the 30 ns conditioning period, the shape of each RM became markedly non-spherical.

4.3.2 -Equilibration

In addition to eliminating instabilities, the 30 ns equilibration periods brought all 4 simulation systems to apparent equilibrium values for energies and volumes. Therefore, the entire 3 µs-Anton 2 simulations were used for analysis.

4.3.3 -Water Exchange

Microsecond timescale simulations revealed two mechanisms by which components of the RMs exchanged between the two RMs in each system: The first mechanism was observed in all systems, operating continuously throughout the trajectory, and it did not involve contact between RMs (contact-independent). The rate water exchange via this mechanism was similar in all systems and in both directions, even despite differences in RM size (Figure 4.2). Therefore, increases or decreases in RM size were not observed through this contact-independent mechanism.

The second mechanism was only observed in the ***NN*** and ***NNp*** systems, only after 2 μs, and involved not only contact, but transient fusion of two RMs (contact-dependent). Visual inspection revealed that the contact-dependent exchange involved only small regions on two RM surfaces, rather than whole surface (Figure 4.3), and lasted less than 1 μs. Thus, contact-dependent exchange may be described as the formation of a transient channel through which RM contents may move. Of note, however, the two RMs that resulted after the channel broke down were not equal in size (Table 4.2 and Figure 4.3).

A possible explanation for why some RMs merged and some did not could be differences in the frequency of collision. The short-range attractive interaction (i.e. VdW interaction) energy between the surfactant layers of two RMs was calculated to quantify the frequency of collisions between RMs (Figure 4.4). Because RMs in each system collided multiple times, fusion cannot be a result of more frequent collision.

Another possible explanation for why some RMs merged and some did not may be differences in AOT energies (see Chapter 2). For example, the AOT energies of the ***S*** and ***L*** systems are more positive than that of the N systems (Figure 4.5). When the RMs fuse, AOT energies tend to become much more negative. However, these differences require further analysis, and simulation of the NN system is ongoing to observe the process of fission following fusion.

4.4 -Discussion

Chapter 2 provided quantitative insight into the relationship between W_0 and the size of a protein-free RM in the commonly used water/AOT/isooctane system, while this chapter examined the properties of RM pairs and protein-containing RMs. These studies to this point demonstrate that RM simulations must be extended to the microsecond timescale to observe phenomena that are critical to the determination of their size, shape, and other properties. In particular, the mechanism underlying water exchange appears to involve partial fusion or channel formation – a phenomenon anticipated by experimental investigators, but not observed in simulation until now.

Table 4.1 - Compositions of simulated systems*

System Name		n_{water}	n_{sod}	n_{AOT}	n_{ISO}	n_{atoms}	f_{iso} (%)	s (Å)
NN	N_1	1448	127	127	10070	287272	87	130 x 165 x 130
	N_2	1448	127	127				
NS	N	1448	127	127	10070	280876	90	130 x 165 x 130
	S	724	63	63				
NL	N	1448	127	127	7500	226764	81	130 x 150 x 130
	L	2166	190	190				
NNp	N	1448	127	127	7000	208053	83	130 x 145 x 130
	Np	1448	130	127				

*n_{water}, n_{sod}, n_{AOT}, n_{ISO}, and n_{atoms} are the numbers of water molecules, sodium cations, AOT, isooctane molecules. n_{atoms} is the total number of atoms in each system. f_{iso} is the mass fraction of isoO as a percentage of mass of all components in the system. s is edge length of the unit cell.

Table 4.2 - Compositions of resulting RMs in the *NN* and the *NNp* systems after merging and splitting*

System Name		n_{water}	n_{sod}	n_{AOT}	W_0
NN	RM	1108	109	101	11
	RM	1788	145	153	11.7
NNp	RM(p)	2296	195	191	12
	RM	600	62	63	9.5

*n_{water}, n_{sod}, and n_{AOT} are the numbers of water molecules, sodium cations, AOT in resulting RMs after merging and splitting. W_0 is water loading ratio in these forming RMs.

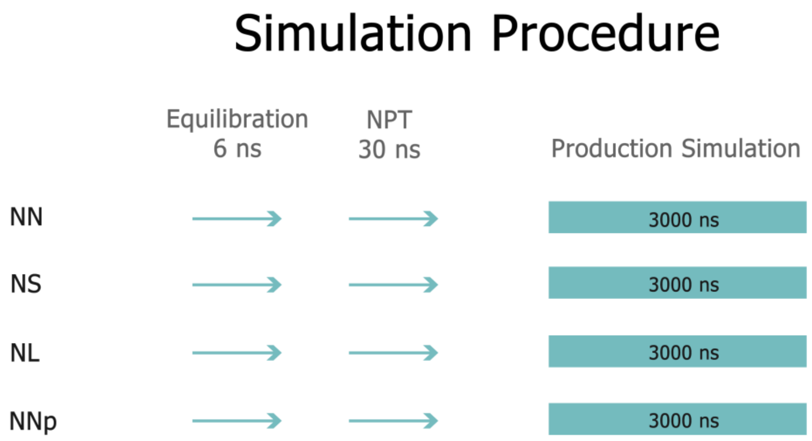

Figure 4.1 - Simulation procedure followed for 4 systems.

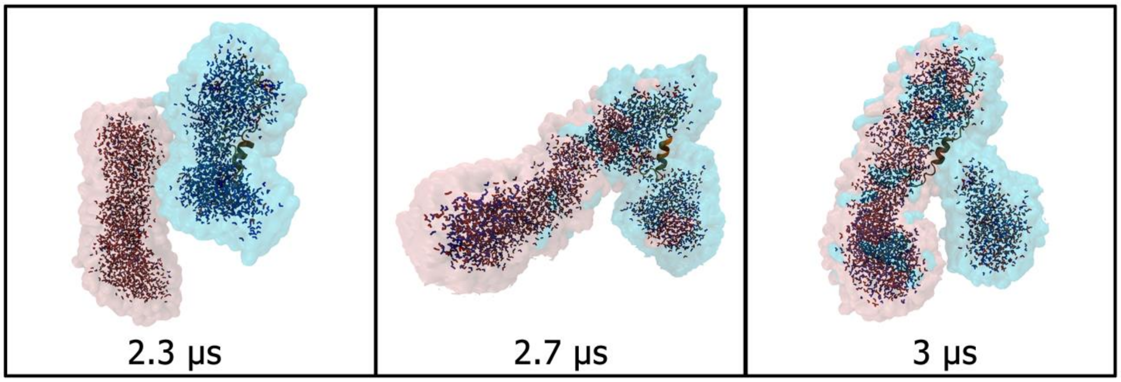

Figure 4.2 - Collided *N* and *Np* (left), merged *N* and *Np* (middle), and a possible splitting that would result in formation of one protein-containing RM with W_0= 12 and one protein-free RM with W_0=9.5 (right).
The structure is illustrated by representing water with licorice (red: ***N*** and blue: ***Np***) model, peptide as orange cartoon, AOT molecules as transparent surfaces (pink: ***N*** and cyan: ***Np***).

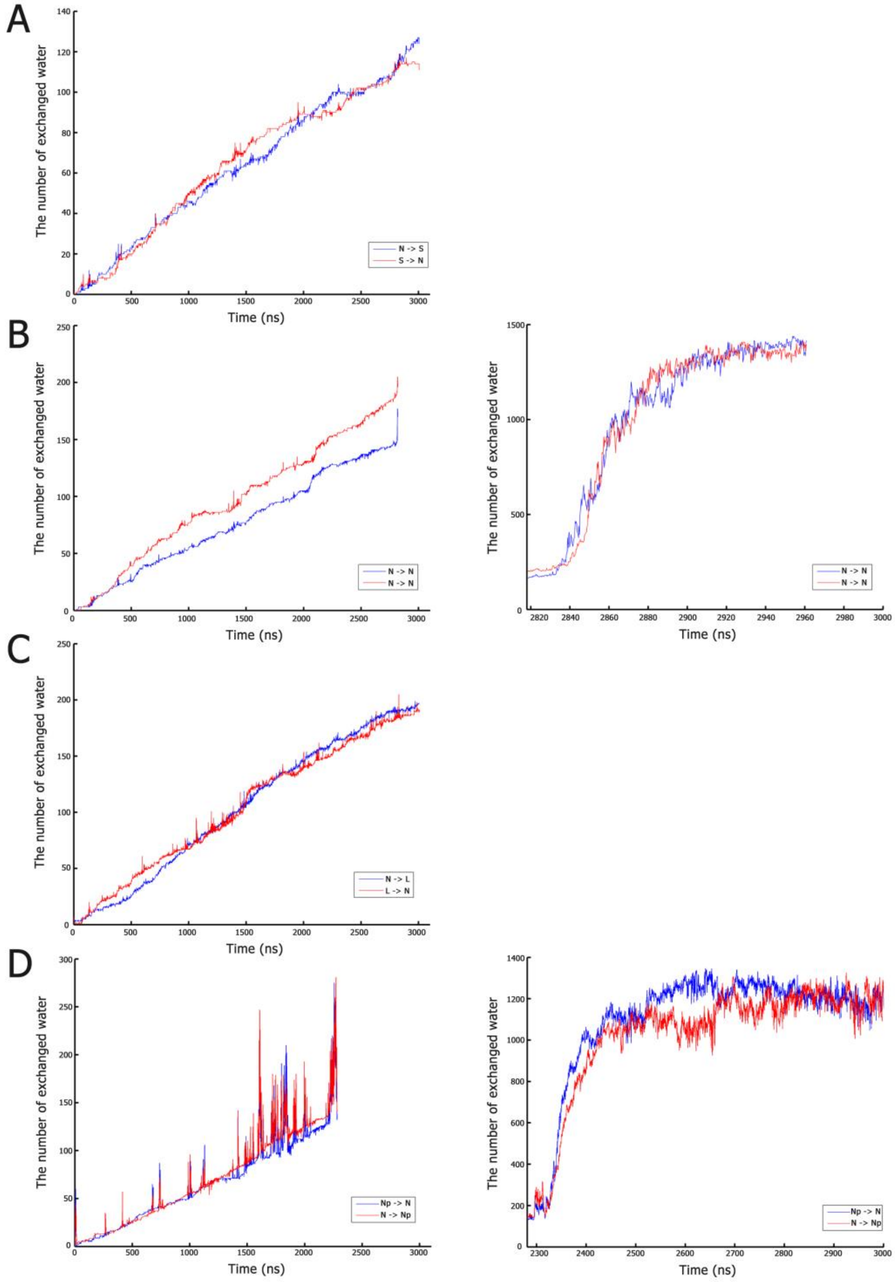

Figure 4.3 - The number of water transferred between two RMs of same system. (A) The ***NS*** system, (B) The ***NN*** system before merging (left) and merging (right), (C) The ***NL*** system, (D) The ***NNp*** system before merging (left) and merging (right).

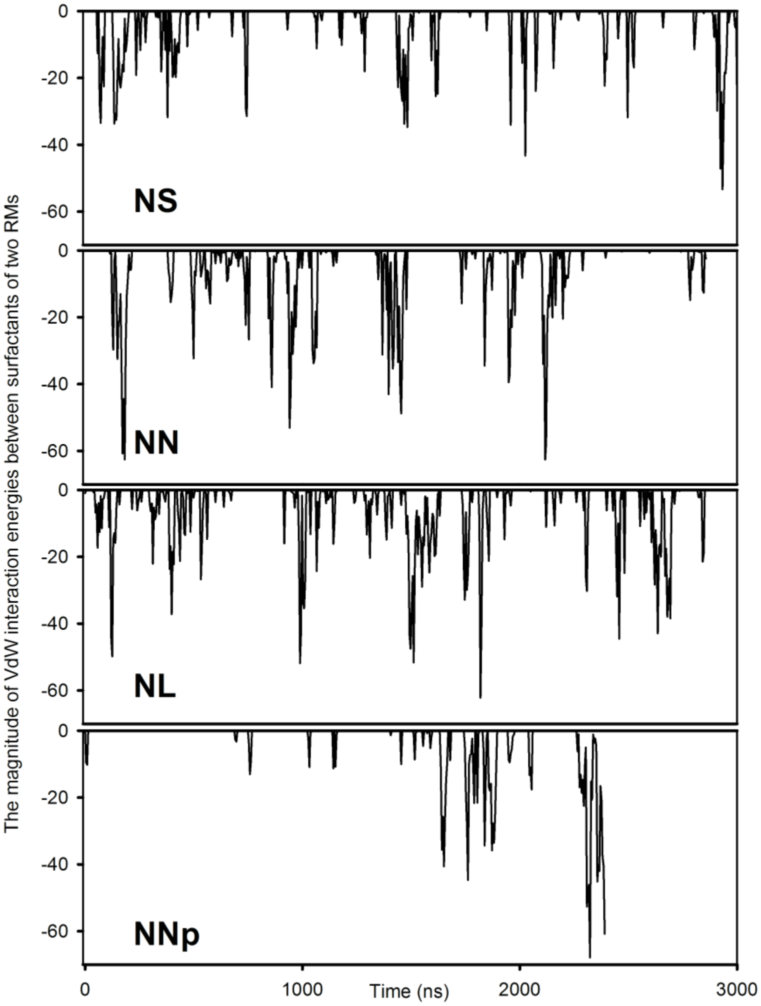

Figure 4.4 - VdW interaction energies between surfactant layers of two RMs in the same system.

Non-zero energies indicate collisions between RMs of the same system. (A) ***NS*** system, (B) ***NN*** system, (C) ***NL*** system, (D) ***NNp*** system.

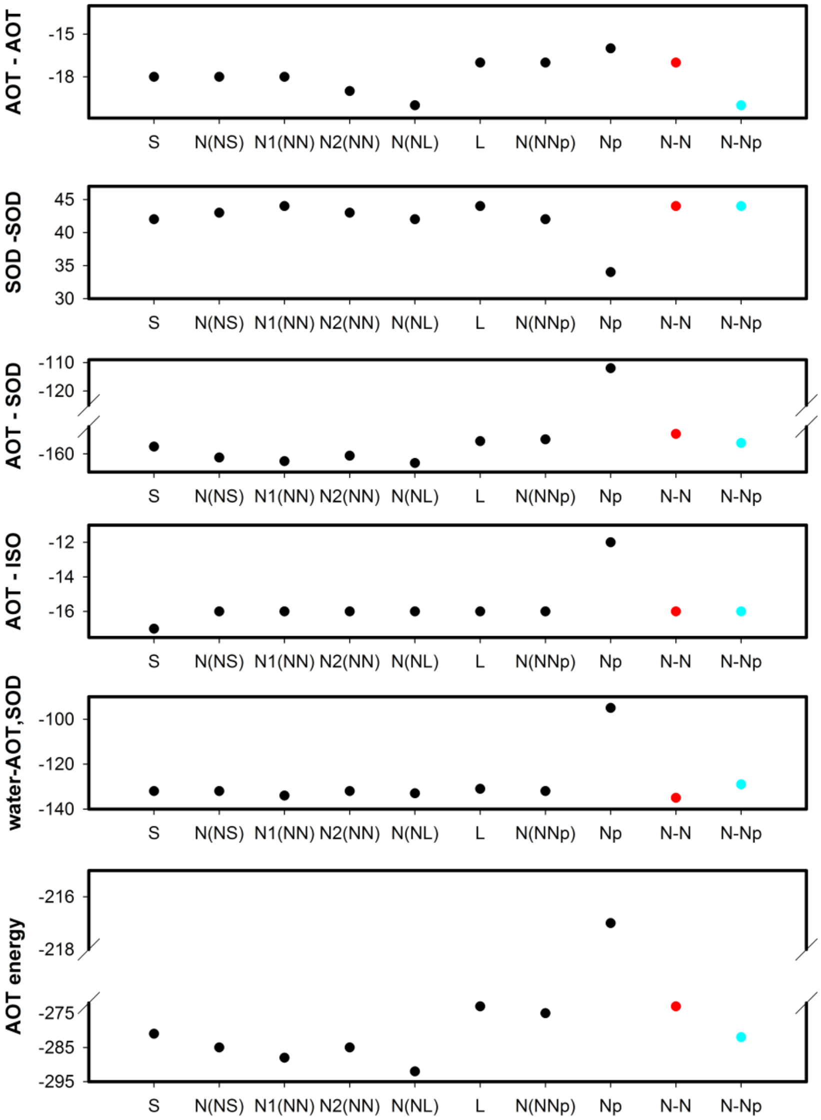

Figure 4.5 - RM system nonbonded interaction energies in kcal/mol, normalized by n_{AOT}.
(N(NS) is the normal size RM in the ***NS*** system; N1(NN) and N2(NN) are normal size RMs in the ***NN*** system; N(NL) is the normal size RM in the ***NL*** system; N(NNp) is the normal size RM in the ***NNp*** system; N-N and N-Np are merged structures in the ***NN*** and ***NNp*** systems. "AOT energy" is the sum of the energies depicted in upper panels.)

Chapter 5: Summary and Future Directions

One of the important pathological hallmarks of AD is cerebral plaques of Aβ protein fibrils which are natural products of metabolism consisting of 39 to 43 amino acids. It has been proposed that an imbalance between production and clearance causes Aβ accumulation, fibril formation, and the development of amyloid plaques in AD (Tanzi & Bertram, 2005). However, a key event, often overlooked, is the circumstances that nucleate fibril formation. Monomeric Aβ proteins have no fixed structure (they are "intrinsically disordered"). There are as-yet-unknown factors that cause monomeric Aβ proteins to fold into extended β structure and these factors must be understood before this fundamental feature of AD pathogenesis may be understood.

It has been shown that Aβ40 monomers can adopt a structure that is similar to fibrils under the conditions that exist in an RM (Yeung & Axelsen, 2012). In this work, MD simulations were pursued in an effort to understand the interactions between Aβ40 and RMs, and the structure that gives rise to the experimental findings. Prerequisite to proper simulations of polypeptides encapsulated in RMs, however, fundamental aspects of RM behavior and protein encapsulation required further development. Therefore, this research has two distinct components: development of a valid computational RM model, and comparison of simulated results from an RM-encapsulated polypeptide to experimental results on an identical system.

We demonstrated that RM size is most likely determined by a minimum overall interaction energy per surfactant for any given W_0. Consequently, we expected to find that RMs that are too small or too large for any given W_0 value would have excess internal energy that drives mass exchange and changes in RM shape. However, the results in Chapter 4 appear to contradict this hypothesis, at least on the time scale over which we could observe. Further studies are planned to determine whether other factors determine RM size, or whether results over a longer timescale will be consistent with this hypothesis.

In Chapter 3, we hypothesized that remarkable structure of encapsulated Aβ40 is induced by confinement, crowding, high ionic strength, and/or the interaction of specific residues with interior surface of the RM. To test this hypothesis, we created a computational model of the same system used in the experimental study of encapsulated Aβ40. Our results were consistent with experimental findings, and demonstrated three important factors: specific interactions between the surfactant layer and central hydrophobic cluster of the polypeptide, high ionic strength inducing the formation of intramolecular hydrogen bonds, and interactions between polypeptide and the surfactant layer that induced large-scale distortions in RM shape. On the basis of these findings, a new mechanism is proposed whereby membranes nucleate fibril formation and facilitate the in-register alignment of polypeptide strands with extended beta structure that is characteristic of amyloid fibrils.

BIBLIOGRAPHY

The PyMOL Molecular Graphics System. Version 1.8. (2016). Schrödinger, LLC.

Ref Type: Generic

Abel, S., Sterpone, F., Bandyopadhyay, S., & Marchi, M. (2004). Molecular modeling and simulations of AOT-Water reverse micelles in isooctane: Structural and dynamic properties. *Journal of Physical Chemistry B, 108,* 19458-19466.

Abel, S., Waks, M., & Marchi, M. (2010). Molecular dynamics simulations of cytochrome c unfolding in AOT reverse micelles: The first steps. *European Physical Journal e, 32,* 399-409.

Almgren, M., Johannsson, R., & Eriksson, J. C. (1993). Polydispersity of Aot Droplets Measured by Time-Resolved Fluorescence Quenching. *Journal of Physical Chemistry, 97,* 8590-8594.

Amararene, A., Gindre, M., Le Huerou, J. Y., Urbach, W., Valdez, D., & Waks, M. (2000). Adiabatic compressibility of AOT [sodium bis(2-ethylhexyl)sulfosuccinate] reverse micelles: Analysis of a simple model based an micellar size and volumetric measurements. *Physical Review E, 61,* 682-689.

Antzutkin, O. N., Balbach, J. J., Leapman, R. D., Rizzo, N. W., Reed, J., & Tycko, R. (2000). Multiple quantum solid-state NMR indicates a parallel, not antiparallel, organization of beta-sheets in Alzheimer's beta-amyloid fibrils. *Proceedings of the National Academy of Sciences USA, 97,* 13045-13050.

Bera, S., Korshavn, K. J., Kar, R. K., Lim, M. H., Ramamoorthy, A., & Bhunia, A. (2016). Biophysical insights into the membrane interaction of the core amyloid-forming A beta(40) fragment K16-K28 and its role in the pathogenesis of Alzheimer's disease. *Physical Chemistry Chemical Physics, 18,* 16890-16901.

Berendsen, H. J. C., Vanderspoel, D., & Vandrunen, R. (1995). Gromacs - A Message-Passing Parallel Molecular-Dynamics Implementation. *Computer Physics Communications, 91,* 43-56.

Bernstein, S. L., Wyttenbach, T., Baumketnert, A., Shea, J. E., Bitan, G., Teplow, D. B. et al. (2005). Amyloid beta-protein: Monomer structure and early aggregation states of A beta 42 and its Pro(19) alloform. *Journal of the American Chemical Society, 127,* 2075-2084.

Bohidar, H. B. & Behboudnia, M. (2001). Characterization of reverse micelles by dynamic light scattering. *Colloids and Surfaces A-Physicochemical and Engineering Aspects, 178,* 313-323.

Brodskaya, E. N. & Mudzhikova, G. V. (2006). Molecular dynamics simulation of AOT reverse micelles. *Mol.Phys., 104,* 3635-3643.

Brown, A. M. & Bevan, D. R. (2016). Molecular Dynamics Simulations of Amyloid beta-Peptide (1-42): Tetramer Formation and Membrane Interactions. *Biophysical Journal, 111,* 937-949.

Burley, S. K. & Petsko, G. A. (1985). Aromatic-Aromatic Interaction: A Mechanism of Protein Structure Stabilization. *Science, 229,* 23-28.

Burley, S. K. & Petsko, G. A. (1986). Amino-aromatic interactions in proteins. *FEBS Lett., 203,* 139-143.

Chang, Q. L., Liu, H. H., & Chen, J. Y. (1994). Fourier transform infrared spectra studies of protein in reverse micelles: effect of AOT/isooctane on the secondary structure of [alpha]-chymotrypsin. *Biochimica et Biophysica Acta (BBA) - Protein Structure and Molecular Enzymology, 1206,* 247-252.

Chatenay, D., Urbach, W., Nicot, C., Vacher, M., & Waks, M. (1987). Hydrodynamic Radii of Protein-Free and Protein-Containing Reverse Micelles As Studied by Fluorescence Recovery After Fringe Photobleaching - Perturbations Introduced by Myelin Basic-Protein Uptake. *Journal of Physical Chemistry, 91,* 2198-2201.

Chowdhary, J. & Ladanyi, B. M. (2009). Molecular Dynamics Simulation of Aerosol-OT Reverse Micelles. *Journal of Physical Chemistry B, 113,* 15029-15039.

Cringus, D., Bakulin, A., Lindner, J., Vohringer, P., Pshenichnikov, M. S., & Wiersma, D. A. (2007). Ultrafast energy transfer in water-AOT reverse micelles. *Journal of Physical Chemistry B, 111,* 14193-14207.

Cukalevski, R., Boland, B., Frohm, B., Thulin, E., Walsh, D., & Linse, S. (2012). Role of Aromatic Side Chains in Amyloid β-Protein Aggregation. *ACS Chemical Neuroscience*.

Darden, T., York, D., & Pedersen, L. (1993). Particle Mesh Ewald - An N.Log(N) Method for Ewald Sums in Large Systems. *Journal of Chemical Physics, 98,* 10089-10092.

Davis, C. H. & Berkowitz, M. L. (2009a). Interaction Between Amyloid-beta (1-42) Peptide and Phospholipid Bilayers: A Molecular Dynamics Study. *Biophysical Journal, 96,* 785-797.

Davis, C. H. & Berkowitz, M. L. (2009b). Structure of the Amyloid-beta (1-42) Monomer Absorbed To Model Phospholipid Bilayers: A Molecular Dynamics Study. *Journal of Physical Chemistry B, 113,* 14480-14486.

Di Scala, C., Yahi, N., Lelievre, C., Garmy, N., Chahinian, H., & Fantini, J. (2013). Biochemical Identification of a Linear Cholesterol-Binding Domain within Alzheimer's beta Amyloid Peptide. *ACS Chemical Neuroscience, 4,* 509-517.

Du, C. F., He, W., Yin, T. X., & Shen, W. G. (2014). Volumetric Properties of Water/AOT/Isooctane Microemulsions. *Langmuir, 30,* 15135-15142.

Eicke, H. F. & Rehak, J. (1976). Formation of Water-Oil-Microemulsions. *Helvetica Chimica Acta, 59,* 2883-2891.

Ellis, R. J. & Minton, A. P. (2006). Protein aggregation in crowded environments. *Biological Chemistry, 387,* 485-497.

Eskici, G. & Axelsen, P. H. (2016). The Size of AOT Reverse Micelles. *Journal of Physical Chemistry B, 120,* 11337-11347.

Esler, W. P., Stimson, E. R., Ghilardi, J. R., Lu, Y. A., Felix, A. M., Vinters, H. V. et al. (1996). Point substitution in the central hydrophobic cluster of a human beta-amyloid congener disrupts peptide folding and abolishes plaque competence. *Biochemistry, 35,* 13914-13921.

Faeder, J. & Ladanyi, B. M. (2000). Molecular dynamics simulations of the interior of aqueous reverse micelles. *Journal of Physical Chemistry B, 104,* 1033-1046.

Faeder, J. & Ladanyi, B. M. (2001). Solvation dynamics in aqueous reverse micelles: A computer simulation study. *Journal of Physical Chemistry B, 105,* 11148-11158.

Faeder, J. & Ladanyi, B. M. (2005). Solvation dynamics in reverse micelles: The role of headgroup-solute interactions. *Journal of Physical Chemistry B, 109,* 6732-6740.

Farago, B., Richter, D., Huang, J. S., Safran, S. A., & Milner, S. T. (1990). Shape and Size Fluctuations of Microemulsion Droplets - the Role of Cosurfactant. *Physical Review Letters, 65,* 3348-3351.

Fayer, M. D. (2011). Water in a Crowd. *Physiology, 26,* 381-392.

Feller, S. E., Zhang, Y., Pastor, R. W., & Brooks, B. R. (1995). Constant pressure molecular dynamics simulation: the Langevin piston method. *Journal of Chemical Physics, 103,* 4613-4621.

Fezoui, Y. & Teplow, D. B. (2002). Kinetic studies of amyloid beta-protein fibril assembly - Differential effects of alpha-helix stabilization. *Journal of Biological Chemistry, 277,* 36948-36954.

Fletcher, P. D. I., Howe, A. M., & Robinson, B. H. (1987). The Kinetics of Solubilisate Exchange Between Water Droplets of A Water-In-Oil Microemulsion. *Journal of the Chemical Society-Faraday Transactions I, 83,* 985-1006.

Foloppe, N. & MacKerell, A. D., Jr. (2000). All-atom empirical force field for nucleic acids: I. Parameter optimization based on small molecule and condensed phase macromolecular target data. *Journal of Computational Chemistry, 21,* 86-104.

Fragoso, A., Pacheco, R., & Karmali, A. (2012). Investigation of structural effects and behaviour of Pseudomonas aeruginosa amidase encapsulated in reversed micelles. *Process Biochemistry, 47,* 264-272.

Fuglestad, B., Gupta, K., Wand, A. J., & Sharp, K. A. (2016). Characterization of Cetyltrimethylammonium Bromide/Hexanol Reverse Micelles by Experimentally Benchmarked Molecular Dynamics Simulations. *Langmuir, 32,* 1674-1684.

Fulton, A. B. (1982). How Crowded Is the Cytoplasm. *Cell, 30,* 345-347.

Gnanakaran, S., Nussinov, R., & Garcia, A. E. (2006). Atomic-level description of amyloid beta-dimer formation. *Journal of the American Chemical Society, 128,* 2158-2159.

Goh, G. B., Eike, D. M., Murch, B. P., & Brooks, C. L. (2015). Accurate Modeling of Ionic Surfactants at High Concentration. *The Journal of Physical Chemistry B, 119,* 6217-6224.

Haass, C. & Selkoe, D. J. (2007). Soluble protein oligomers in neurodegeneration: lessons from the Alzheimer's amyloid beta-peptide. *Nature Reviews Molecular Cell Biology, 8,* 101-112.

Hirai, M., Kawaihirai, R., Yabuki, S., Takizawa, T., Hirai, T., Kobayashi, K. et al. (1995). Aerosol-Ot Reversed Micellar Formation at Low Water-Surfactant Ratio Studied by Synchrotron-Radiation Small-Angle X-Ray-Scattering. *Journal of Physical Chemistry, 99,* 6652-6660.

Hou, L. M., Shao, H. Y., Zhang, Y. B., Li, H., Menon, N. K., Neuhaus, E. B. et al. (2004). Solution NMR studies of the A beta(1-40) and A beta(1-42) peptides establish that the met35 oxidation state affects the mechanism of amyloid formation. *Journal of the American Chemical Society, 126,* 1992-2005.

Howe, A. M., Mcdonald, J. A., & Robinson, B. H. (1987). Fluorescence Quenching As A Probe of Size Domains and Critical Fluctuations in Water-In-Oil Microemulsions. *Journal of the Chemical Society-Faraday Transactions I, 83,* 1007-1027.

Humphrey, W., Dalke, A., & Schulten, K. (1996). VMD: Visual molecular dynamics. *Journal of Molecular Graphics & Modelling, 14,* 33-38.

Jada, A., LANG, J., & Zana, R. (1989). Relation Between Electrical Percolation and Rate-Constant for Exchange of Material Between Droplets in Water in Oil Microemulsions. *J.Phys.Chem., 93,* 10-12.

Jarvet, J., Damberg, P., Bodell, K., Eriksson, L. E. G., & Graslund, A. (2000). Reversible random coil to beta-sheet transition and the early stage of aggregation of the A beta(12-28) fragment from the Alzheimer peptide. *Journal of the American Chemical Society, 122,* 4261-4268.

Jorgensen, W. L., Chandrasekhar, J., Madura, J. D., Impey, R. W., & Klein, M. L. (1983). Comparison of simple potential functions for simulating liquid water. *Journal of Chemical Physics, 79,* 926-935.

Kinugasa, T., Kondo, A., Nishimura, S., Miyauchi, Y., Nishii, Y., Watanabe, K. et al. (2002). Estimation for size of reverse micelles formed by AOT and SDEHP based on viscosity measurement. *Colloids and Surfaces A-Physicochemical and Engineering Aspects, 204,* 193-199.

Kirkitadze, M. D., Condron, M. M., & Teplow, D. B. (2001). Identification and characterization of key kinetic intermediates in amyloid beta-protein fibrillogenesis. *Journal of Molecular Biology, 312,* 1103-1119.

Kotlarchyk, M., Chen, S. H., & Huang, J. S. (1982). Temperature-Dependence of Size and Polydispersity in A 3-Component Micro-Emulsion by Small-Angle Neutron-Scattering. *Journal of Physical Chemistry, 86,* 3273-3276.

Kotlarchyk, M., Chen, S. H., Huang, J. S., & Kim, M. W. (1984). Structure of 3-Component Microemulsions in the Critical Region Determined by Small-Angle Neutron-Scattering. *Physical Review A, 29,* 2054-2069.

Kremer, J. J., Pallitto, M. M., Sklansky, D. J., & Murphy, R. M. (2000). Correlation of β-Amyloid Aggregate Size and Hydrophobicity with Decreased Bilayer Fluidity of Model Membranes. *Biochemistry, 39,* 10309-10318.

Kremer, J. J., Sklansky, D. J., & Murphy, R. M. (2001). Profile of changes in lipid bilayer structure caused by beta- amyloid peptide. *Biochemistry, 40,* 8563-8571.

Lemkul, J. A. & Bevan, D. R. (2008). A comparative molecular dynamics analysis of the amyloid beta-peptide in a lipid bilayer. *Archives of Biochemistry and Biophysics, 470,* 54-63.

Lemkul, J. A. & Bevan, D. R. (2009). Perturbation of membranes by the amyloid beta-peptide - a molecular dynamics study. *FEBS Journal, 276,* 3060-3075.

Lemkul, J. A. & Bevan, D. R. (2011). Lipid composition influences the release of Alzheimer's amyloid beta-peptide from membranes. *Protein Science, 20,* 1530-1545.

Lemkul, J. A. & Bevan, D. R. (2013). Aggregation of Alzheimer's Amyloid β-Peptide in Biological Membranes: A Molecular Dynamics Study. *Biochemistry*.

Lomakin, A., Chung, D. S., Benedek, G. B., Kirschner, D. A., & Teplow, D. B. (1996). On the nucleation and growth of amyloid beta-protein fibrils: Detection of nuclei and quantitation of rate constants. *Proceedings of the National Academy of Sciences USA, 93,* 1125-1129.

Luby-Phelps, K. (2000). Cytoarchitecture and physical properties of cytoplasm: Volume, viscosity. diffusion, intracellular surface area. *International Review of Cytology - A Survey of Cell Biology, Vol 192, 192,* 189-221.

MacKerell, A. D., Jr., Bashford, D., Bellott, M., Dunbrack, R. L., Evanseck, J. D., Field, M. J. et al. (1998). All-atom empirical potential for molecular modeling and dynamics studies of proteins. *Journal of Physical Chemistry B, 102,* 3586-3616.

MacKerell, A. D., Bashford, D., Bellott, M., Dunbrack, R. L., Evanseck, J. D., Field, M. J. et al. (1998). All-atom empirical potential for molecular modeling and dynamics studies of proteins. *Journal of Physical Chemistry B, 102,* 3586-3616.

MacKerell, A. D., Wiorkiewiczkuczera, J., & Karplus, M. (1995). An All-Atom Empirical Energy Function for the Simulation of Nucleic-Acids. *Journal of the American Chemical Society, 117,* 11946-11975.

Maitra, A. (1984). Determination of Size Parameters of Water Aerosol Ot Oil Reverse Micelles from Their Nuclear Magnetic-Resonance Data. *Journal of Physical Chemistry, 88,* 5122-5125.

Makin, O. S., Atkins, E., Sikorski, P., Johansson, J., & Serpell, L. C. (2005). Molecular basis for amyloid fibril formation and stability. *Proceedings of the National Academy of Sciences USA, 102,* 315-320.

Manna, M. & Mukhopadhyay, C. (2013). Binding, Conformational Transition and Dimerization of Amyloid-beta Peptide on GM1-Containing Ternary Membrane: Insights from Molecular Dynamics Simulation. *PLoS ONE, 8*.

Marchi, M. & Abel, S. (2015). Modeling the Self-Aggregation of Small AOT Reverse Micelles from First-Principles. *Journal of Physical Chemistry Letters, 6,* 170-174.

Martinez, A. V., Malolepsza, E., Rivera, E., Lu, Q., & Straub, J. E. (2014a). Exploring the role of hydration and confinement in the aggregation of amyloidogenic peptides A beta(16-22) and Sup35(7-13) in AOT reverse micelles. *J.Chem.Phys., 141*.

Martinez, A. V., Malolepsza, E., Rivera, E., Lu, Q., & Straub, J. E. (2014b). Exploring the role of hydration and confinement in the aggregation of amyloidogenic peptides A beta(16-22) and Sup35(7-13) in AOT reverse micelles. *Journal of Chemical Physics, 141*.

Martinez, A. V., Dominguez, L., Malolepsza, E., Moser, A., Ziegler, Z., & Straub, J. E. (2013). Probing the Structure and Dynamics of Confined Water in AOT Reverse Micelles. *Journal of Physical Chemistry B, 117,* 7345-7351.

McLaurin, J. & Chakrabartty, A. (1997). Characterization of the interactions of Alzheimer beta-amyloid peptides with phospholipid membranes. *European Journal of Biochemistry, 245,* 355-363.

Meersman, F., Dirix, C., Shipovskov, S., Klyachko, N. L., & Heremans, K. (2005). Pressure-induced protein unfolding in the ternary system AOT-octane-water is different from that in bulk water. *Langmuir, 21,* 3599-3604.

Minton, A. P. (2000). Implications of macromolecular crowding for protein assembly. *Current Opinion in Structural Biology, 10,* 34-39.

Minton, A. P. (2001). The influence of macromolecular crowding and macromolecular confinement on biochemical reactions in physiological media. *Journal of Biological Chemistry, 276,* 10577-10580.

Mobley, D. L., Cox, D. L., Singh, R. R. P., Maddox, M. W., & Longo, M. L. (2004). Modeling amyloid beta-peptide insertion into lipid bilayers. *Biophysical Journal, 86,* 3585-3597.

Moilanen, D. E., Fenn, E. E., Wong, D., & Fayer, M. D. (2009). Water dynamics in large and small reverse micelles: From two ensembles to collective behavior. *Journal of Chemical Physics, 131,* 014704.

Mori, H., Takio, K., Ogawara, M., & Selkoe, D. J. (1992). Mass spectrometry of purified amyloid beta protein in Alzheimer's disease. *Journal of Biological Chemistry, 267,* 17082-17086.

Mukherjee, S., Chowdhury, P., & Gai, F. (2007). Infrared study of the effect of hydration on the amide I band and aggregation properties of helical peptides. *Journal of Physical Chemistry B, 111,* 4596-4602.

Nazario, L. M. M., Hatton, T. A., & Crespo, J. P. S. G. (1996). Nonionic cosurfactants in AOT reversed micelles: Effect on percolation, size, and solubilization site. *Langmuir, 12,* 6326-6335.

Pal, N., Verma, S. D., Singh, M. K., & Sen, S. (2011). Fluorescence Correlation Spectroscopy: An Efficient Tool for Measuring Size, Size-Distribution and Polydispersity of Microemulsion Droplets in Solution. *Analytical Chemistry, 83,* 7736-7744.

Peterson, R. W., Anbalagan, K., Tommos, C., & Wand, A. J. (2004). Forced folding and structural analysis of metastable proteins. *Journal of the American Chemical Society, 126,* 9498-9499.

Phillips, J. C., Braun, R., Wang, W., Gumbart, J., Tajkhorshid, E., Villa, E. et al. (2005). Scalable molecular dynamics with NAMD. *Journal of Computational Chemistry, 26,* 1781-1802.

Pomata, M. H. H., Laria, D., Skaf, M. S., & Elola, M. D. (2008). Molecular dynamics simulations of AOT-water/formamide reverse micelles: Structural and dynamical properties. *J.Chem.Phys., 129*.

Ricka, J., Borkovec, M., & Hofmeier, U. (1991). Coated Droplet Model of Microemulsions - Optical Matching and Polydispersity. *Journal of Chemical Physics, 94,* 8503-8509.

Robertus, C., Philipse, W. H., Joosten, J. G. H., & Levine, Y. K. (1989). Solution of the Percus-Yevick Approximation of the Multicomponent Adhesive Spheres System Applied to the Small-Angle X-Ray-Scattering from Microemulsions. *J.Chem.Phys., 90,* 4482-4490.

Robinson, B. H., Toprakcioglu, C., Dore, J. C., & Chieux, P. (1984). Small-Angle Neutron-Scattering Study of Microemulsions Stabilized by Aerosol-Ot .1. Solvent and Concentration Variation. *Journal of the Chemical Society-Faraday Transactions I, 80,* 13-27.

Rodriguez, J., Marti, J., Guardia, E., & Laria, D. (2007). Protons in non-ionic aqueous reverse micelles. *J.Phys.Chem.B, 111,* 4432-4439.

Rosenfeld, D. E. & Schmuttenmaer, C. A. (2006). Dynamics of water confined within reverse micelles. *J.Phys.Chem.B, 110,* 14304-14312.

Rosenfeld, D. E. & Schmuttenmaer, C. A. (2011). Dynamics of the Water Hydrogen Bond Network at Ionic, Nonionic, and Hydrophobic Interfaces in Nanopores and Reverse Micelles. *J.Phys.Chem.B, 115,* 1021-1031.

Sabate, R. & Estelrich, J. (2005). Evidence of the existence of micelles in the fibrillogenesis of beta-amyloid peptide. *Journal of Physical Chemistry B, 109,* 11027-11032.

Sabate, R., Gallardo, M., & Estelrich, J. (2005). Spontaneous incorporation of beta-amyloid peptide into neutral liposomes. *Colloids and Surfaces A-Physicochemical and Engineering Aspects, 270,* 13-17.

Seubert, P., VigoPelfrey, C., Esch, F., Lee, M., Dovey, H., Davis, D. et al. (1992). Isolation and Quantification of Soluble Alzheimers Beta-Peptide from Biological-Fluids. *Nature, 359,* 325-327.

Shan, Y. B., Klepeis, J. L., Eastwood, M. P., Dror, R. O., & Shaw, D. E. (2005). Gaussian split Ewald: A fast Ewald mesh method for molecular simulation. *Journal of Chemical Physics, 122*.

Shaw, D. E., Deneroff, M. M., Dror, R. O., Kuskin, J. S., Larson, R. H., Salmon, J. K. et al. (2008). Anton, a special-purpose machine for molecular dynamics simulation. *Communications of the Acm, 51,* 91-97.

Shaw, D. E., Dror, R. O., Salmon, J. K., & Grossman, J. P. (11-20-2009). Millisecond-Scale Molecular Dynamics Simulations on Anton. Mackenzie, K. M. and Banka, J. A. Proceedings of the ACM/IEEE Conference on Supercomputing (SC09) . Portland, Oregon.

Ref Type: Generic

Shaw, D. E., Grossman, J. P., Bank, J. P., Batson, B., Butts, J. A., Chao, J. C. et al. (2014). Anton 2: raising the bar for performance and programmability in a special-purpose molecular dynamics supercomputer. *IEEE, 2014,* 41-53.

Sikorski, P., Atkins, E. D. T., & Serpell, L. C. (2003). Structure and texture of fibrous crystals formed by Alzheimer's A beta(11-25) peptide fragment. *Structure, 11,* 915-926.

Soreghan, B., Kosmoski, J., & Glabe, C. (1994). Surfactant Properties of Alzheimers A-Beta Peptides and the Mechanism of Amyloid Aggregation. *Journal of Biological Chemistry, 269,* 28551-28554.

Tanzi, R. E. & Bertram, L. (2005). Twenty years of the Alzheimer's disease amyloid hypothesis: A genetic perspective. *Cell, 120,* 545-555.

Terzi, E., Holzemann, G., & Seelig, J. (1995). Self-association of beta-amyloid peptide (1-40) in solution and binding to lipid membranes. *Journal of Molecular Biology, 252,* 633-642.

Terzi, E., Holzemann, G., & Seelig, J. (1997). Interaction of Alzheimer beta-amyloid peptide(1-40) with lipid membranes. *Biochemistry, 36,* 14845-14852.

Tian, J. H. & Garcia, A. E. (2011a). Simulations of the confinement of ubiquitin in self-assembled reverse micelles. *J.Chem.Phys., 134*.

Tian, J. H. & Garcia, A. E. (2011b). Simulations of the confinement of ubiquitin in self-assembled reverse micelles. *Journal of Chemical Physics, 134*.

Towns, J., Cockerill, T., Dahan, M., Foster, I., Gaither, K., Grimshaw, A. et al. (2014). XSEDE: Accelerating Scientific Discovery. *Computing in Science & Engineering, 16,* 62-74.

van Holde, K. E., Johnson, W. C., & Ho, P. S. (2006). *Principles of Physical Biochemistry 2nd Ed*. Upper Saddle River, N.J.: Pearson Prentice Hall.

Vandijk, M. A., Joosten, J. G. H., Levine, Y. K., & Bedeaux, D. (1989). Dielectric Study of Temperature-Dependent Aerosol Ot/Water Isooctane Microemulsion Structure. *Journal of Physical Chemistry, 93,* 2506-2512.

Vasquez, V. R., Williams, B. C., & Graeve, O. A. (2011). Stability and Comparative Analysis of AOT/Water/Isooctane Reverse Micelle System Using Dynamic Light Scattering and Molecular Dynamics. *Journal of Physical Chemistry B, 115,* 2979-2987.

Vierros, S. & Sammalkorpi, M. (2015). Phosphatidylcholine reverse micelles on the wrong track in molecular dynamics simulations of phospholipids in an organic solvent. *Journal of Chemical Physics, 142,* 094902.

Walde, P., Giuliani, A. M., Boicelli, C. A., & Luisi, P. L. (1990). Phospholipid-Based Reverse Micelles. *Chemistry and Physics of Lipids, 53,* 265-288.

Walde, P., MAO, Q. C., Bru, R., Luisi, P. L., & Kuboi, R. (1992). pH Artifacts in Reverse Micellar Enzymology - A Warning. *Pure and Applied Chemistry, 64,* 1771-1775.

Wurth, C., Guimard, N. K., & Hecht, M. H. (2002). Mutations that reduce aggregation of the Alzheimer's A beta 42 peptide: an unbiased search for the sequence determinants of A beta amyloidogenesis. *Journal of Molecular Biology, 319,* 1279-1290.

Xu, Y. C., Shen, J. J., Luo, X. M., Zhu, W. L., Chen, K. X., Ma, J. P. et al. (2005). Conformational transition of amyloid beta-peptide. *Proceedings of the National Academy of Sciences of the United States of America, 102,* 5403-5407.

Yan, Y. D. & Clarke, J. H. R. (1990). Dynamic Light-Scattering from Concentrated Water-In-Oil Microemulsions the Coupling of Optical and Size Polydispersity. *J.Chem.Phys., 93,* 4501-4509.

Yano, J., Furedi-Milhofer, H., Wachtel, E., & Garti, N. (2000a). Crystallization of organic compounds in reversed micelles. I. Solubilization of amino acids in water-isooctane-AOT microemulsions. *Langmuir, 16,* 9996-10004.

Yano, J., Furedi-Milhofer, H., Wachtel, E., & Garti, N. (2000b). Crystallization of organic compounds in reversed micelles. II. Crystallization of glycine and l-phenylalanine in water-isooctane-AOT microemulsions. *Langmuir, 16,* 10005-10014.

Yeung, P. S. W. & Axelsen, P. H. (2012). The Crowded Environment of a Reverse Micelle Induces the Formation of beta-Strand Seed Structures for Nucleating Amyloid Fibril Formation. *Journal of the American Chemical Society, 134,* 6061-6063.

Yeung, P. S. W., Eskici, G., & Axelsen, P. H. (2013). Infrared spectroscopy of proteins in reverse micelles. *Biochimica et Biophysica Acta-Biomembranes, 1828,* 2314-2318.

Zhang, S., Iwata, K., Lachenmann, M. J., Peng, J. W., Li, S., Stimson, E. R. et al. (2000). The Alzheimer's peptide A beta adopts a collapsed coil structure in water. *Journal of Structural Biology, 130,* 130-141.

Zhao, L. N., Chiu, S. W., Benoit, J., Chew, L. Y., & Mu, Y. G. (2011). Amyloid beta Peptides Aggregation in a Mixed Membrane Bilayer: A Molecular Dynamics Study. *Journal of Physical Chemistry B, 115,* 12247-12256.

Zhou, H. X. (2008). Protein folding in confined and crowded environments. *Archives of Biochemistry and Biophysics, 469,* 76-82.

Zhou, X. L. & Xu, J. (2012). Free Cholesterol Induces Higher beta-Sheet Content in A beta Peptide Oligomers by Aromatic Interaction with Phe19. *PLoS ONE, 7*.

Zimmerman, S. B. & Trach, S. O. (1991). Estimation of Macromolecule Concentrations and Excluded Volume Effects for the Cytoplasm of Escherichia-Coli. *Journal of Molecular Biology, 222,* 599-620.

Zulauf, M. & Eicke, H. F. (1979). Inverted Micelles and Microemulsions in the Ternary-System H2O-Aerosol-Ot-Isooctane As Studied by Photon Correlation Spectroscopy. *Journal of Physical Chemistry, 83,* 480-486.